Title: Resolved tropical cyclones trigger CO_2 uptake and phytoplankton bloom in an Earth system model simulation

Authors:

David M. Nielsen
david.nielsen@mpimet.mpg.de
Max Planck Institute for Meteorology, Hamburg 20146, Germany

Fatemeh Chegini
University of Hamburg, Hamburg 20146, Germany

Nuno Serra
University of Hamburg, Hamburg 20146, Germany

Arjun Kumar
Max Planck Institute for Meteorology, Hamburg 20146, Germany

Nils Brüggemann
Max Planck Institute for Meteorology, Hamburg 20146, Germany

Cathy Hohenegger
Max Planck Institute for Meteorology, Hamburg 20146, Germany

Tatiana Ilyina
University of Hamburg, Hamburg 20146, Germany
Helmholtz-Zentrum Hereon, Geesthacht 21502, Germany
Max Planck Institute for Meteorology, Hamburg 20146, Germany

Resolved tropical cyclones trigger CO_2 uptake and phytoplankton bloom in an Earth system model simulation

David M. Nielsen[1*], Fatemeh Chegini[2], Nuno Serra[2], Arjun Kumar[1], Nils Brüggemann[1], Cathy Hohenegger[1], and Tatiana Ilyina[1,2,3]

[1]Max Planck Institute for Meteorology, Hamburg, Germany
[2]Universität Hamburg, Hamburg, Germany
[3]Helmholtz-Zentrum Hereon, Geesthacht, Germany
[*]Correspondence to david.nielsen@mpimet.mpg.de

March 18, 2025

Abstract

The ocean carbon cycle is directly impacted by storms in the atmosphere. Tropical cyclones (TCs), particularly, are known to drive intense air-sea CO_2 fluxes and to trigger phytoplankton blooms. However, the latest generation of Earth system models (ESM) cannot realistically represent TCs due to their coarse spatial resolution (typically 100-200 km grid spacing). Here, we present the first km-scale coupled, global, storm- and eddy-resolving (5 km ocean, 5 km atmosphere) ESM simulation including ocean biogeochemistry that is able to resolve TCs, and the cascade of physical-biogeochemical mechanisms that unfold in their response. Our simulated TCs enhance CO_2 fluxes by 20-40 times and cool the surface ocean by 2-3°C, thus contributing to inverting the CO_2 flux direction from ocean outgassing to uptake. Our TCs furthermore trigger a phytoplankton bloom in autumn in the western North Atlantic, which is missed by coarser ESMs. While our TCs boost primary production, they also warm the ocean subsurface, which enhances organic matter remineralization and attenuates their impact on carbon export to depth. Our novel model configuration reproduces mechanisms underlying the ocean carbon cycle variability that remained so far unresolved in ESMs. By representing fine-scale atmosphere-ocean biogeochemistry interactions in our ESM, we pave the way for future work to constrain uncertainties in the role of km-scale events in the ocean carbon cycle at global and climatic scales.

Significance

Earth system models work with relatively low spatial resolution, typically 100-200 km in grid spacing. This is too coarse for the representation of small-scale mechanisms and extreme events, such as intense tropical cyclones (e.g. hurricanes). Nevertheless, such events trigger a number of physical and biological processes that are relevant for climate, but missed by coarser models. Here, we present the first km-scale global Earth system model simulation that resolves interactions between extremely intense cyclones and the ocean carbon cycle with unprecedentedly high resolution (5 km ocean and atmosphere). This will allow future work to reduce uncertainties in the role of km-scale processes in the ocean carbon sink and in its response to a changing climate.

1 Main

The ocean absorbs about 25% of anthropogenic CO_2 emissions every year [1, 2]. However, much of this air-sea exchange of CO_2 is mediated by processes in the surface ocean and atmosphere that are too small to be fully resolved in Earth system models (ESMs). State-of-the-art ESMs, composing the Coupled Model Intercomparison Project (CMIP6) [3] and used to inform the Intergovernmental Panel on Climate Change (IPCC), work with spatial resolution of tens to hundreds of kilometers, which is too coarse to realistically represent tropical cyclones (TCs) [4, 5]. Intense TCs of category 4-5 in the Saffir-Simpson scale (winds $>$ 58 m/s) are particularly misrepresented, or totally absent, in coarse-resolution CMIP6-type models (100-200 km grid spacing) [4, 6]. The higher-resolution subset of CMIP6 models (HighResMIP) [7], reaching up to 25 km in grid spacing, only *"begin to capture some structures of TCs more realistically"* [4], but biases in TC characteristics persist [8, 9]. Here, we present the first coupled storm- and eddy-resolving simulation (5 km ocean, 5 km atmosphere) including the ocean biogeochemistry component HAMOCC (HAMburg Ocean Carbon Cycle) [10] in the ICON (ICOsahedral Non-hydrostatic) model [11]. Our model configuration has been shown to reproduce important TC characteristics, such as intensification rates, core structure [9], and interactions with ocean eddies [12]. Here, we investigate the two *intense* TCs (i.e. category 4 or higher) in the western North Atlantic occurring in our simulation, and their impact on the ocean carbon cycle.

TCs are known to drive high CO_2 fluxes between the ocean and atmosphere [13, 14]. TCs occur about as frequently in ocean outgassing regions as in uptake regions, which mitigates their global annual net effect on the ocean CO_2 uptake [15]. Nevertheless, TCs are responsible for moderating about 20-60% of all air-sea CO_2 exchange in their most prevalent regions and seasons, according to mooring observations and regional modelling studies [16–19], thereby playing an important role in modulating the ocean carbon sink variability. TCs impact the ocean CO_2 sink for weeks after their passage by causing intense ocean heat loss, and hence cooling the surface ocean by 1-6°C [20, 21]. Cooling decreases the ocean partial pressure of CO_2 ($p$$CO_2$) [22], thereby favoring an increasing ocean CO_2 uptake (or decreasing CO_2 outgassing). Therefore, a realistic representation of the impact of TCs on the ocean CO_2 sink must include both their instantaneous and longer-lasting components [15].

A cascade of coupled physical-biogeochemical processes and feedbacks occur in response to TCs. First, not only do air-sea CO_2 fluxes increase exponentially with surface wind speeds [23]. High wind speeds during TC events also mix the upper ocean, contributing to cooling the surface ocean, and warming the subsurface [20, 24]. Ocean mixing also replenishes the sunlit upper oceans with nutrients from below, which enhances marine net primary production by phytoplankton [25–29]. Consequently, intense TCs also mediate the ocean CO_2 sink by enhancing the export of organic carbon to the ocean interior [30]. The phytoplankton bloom following TCs also affects the penetration of shortwave radiation in the ocean, which further amplifies the TC-driven surface cooling effect [31, 32]. Lastly, the cold wake of TCs is observed to negatively feedback on their own intensity and further development [33].

Investigating the impact of km-scale extreme storms on the Earth's climate and carbon cycle remains challenging. Future projections of intense TC impacts, for example, rely on statistical or downscaling techniques [e.g. 34–36], which cannot consistently simulate the feedbacks between scales (i.e. the small scales of TCs and the global and climatic scales) and neither between Earth system components (i.e. ocean-atmosphere feedbacks). Our novel km-scale global ICON configuration is thus an invaluable tool that allows us to resolve ocean-atmosphere interactions triggered by extreme storms within the Earth system in a consistent manner for the first time. We explore the cascade of coupled physical-biogeochemical mechanisms that unfold after the passage of the two intense TCs occurring in the western North Atlantic in our simulations – the first intense TCs ever resolved in a fully coupled global ESM including ocean biogeochemistry. We show how such extreme storms can increase the ocean CO_2 uptake and trigger an autumn phytoplankton bloom in the western North Atlantic.

2 Results and Discussion

Our simulation produces two intense TCs in the western North Atlantic. The first one (TC1) occurs between 1-10 September, and the second one (TC2) occurs between 10-17 September. Both TCs intensify to become hurricanes (i.e. surface wind speeds $\geq$33 m/s) and reach hurricane category

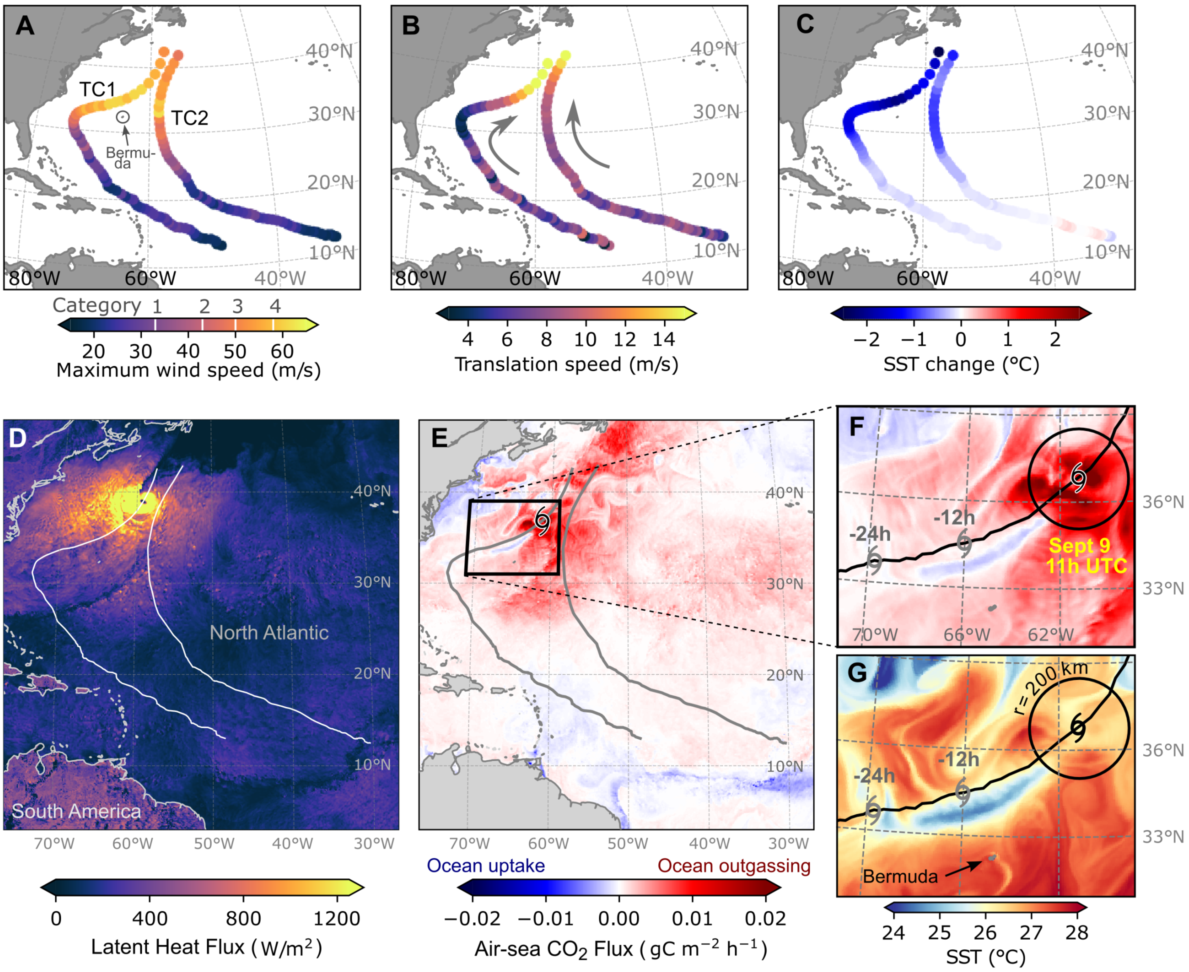

Figure 1: **Simulated tropical cyclones characteristics.** Along-track maximum surface wind speed **(A)**, translation speed **(B)**, and changes in sea surface temperature (SST) due to TC passage **(C)** expressed as differences in SST from 24 hours after minus 24 hours before the TC averaged over a 200 km-radius circle around track points. Track points are spaced by 3 hours in A, B and C for visualization. Maps of surface latent heat flux (LHF, **D**, instantaneous) on 10 September at 16h UTC (12-noon at the longitude of TC1 location), and air-sea CO_2 flux (**E**, hourly mean) at 11h UTC (near TC1 at its maximum intensity). Both LHF and CO_2 fluxes are positive upwards (from ocean to the atmosphere), thus positive values show ocean heat loss and ocean CO_2 outgassing. Zoomed-in views of air-sea CO_2 fluxes **(F)** and SST **(G)**, highlighting the cold wake of TC1 after its maximum intensity. Black cyclone symbols in E, F and G mark the position of TC1 at the time corresponding to the data shown, while grey cyclone symbols mark its previous positions at 12 and 24 hours before.

4 ($\geq$58 m/s) in latitudes north of 30°N (Fig. 1A). Our two TCs follow different paths in the North Atlantic: Both TCs initially travel with a typical north-westward direction, but TC1 takes a sharp turn eastwards after crossing 30°N while intensifying, somewhat similar to 2020 hurricane Paulette [37], but without making landfall in Bermuda. During its sharp turn, TC1 travels with low translation speeds below 6 m/s (Fig. 1B). On the other hand, TC2 follows a predominantly northward track after reaching hurricane intensity, and faster than TC1, with translation speeds always above 6 m/s. Slow translation speeds enable TCs more time to exert sustained wind stress on the ocean [38, 39], leading to enhanced mixing and sea surface cooling.

TC1 cools the surface ocean by up to 2°C, while TC2 cools the surface ocean by about 1°C where wind speed is highest (Fig. 1C). The largest cumulative sea-surface cooling (2-3°C) takes place in the extra-tropics, where the two TC tracks approach each other and their areas of impact overlap (Fig. 2D,F). This is also the warmest region along their tracks, which favors their own intensification. Sea surface cooling is driven by the combined effect of surface heat fluxes and wind-driven vertical diffusion, and only slightly counterbalanced by warm advection (Fig S1, see *'Ocean tracer budget terms'* in Methods). Horizontal advection plays a larger role in warming the wake of TC1, into which the Gulf Stream brings warm tropical waters.

Our simulated TCs yield extreme latent heat fluxes (LHF) of $>$1200 W/m^2 at their maximum wind speeds (Fig. 1D), in line with observations [e.g. 40], and larger than anywhere else on the Earth's surface, which contributes to cooling the surface ocean. For context, maximum surface LHF values in the Amazon forest range in 200-500 W/m^2 during peak incoming solar radiation at noon, when land evaporation and transpiration by vegetation are at largest [41, 42]. Not only do hurricanes drive intense surface heat exchange, but also intense CO_2 exchange rates between the ocean and atmosphere.

2.1 Hurricanes impact the ocean carbon sink

Our simulated TCs impact the ocean CO_2 uptake in two ways. First, TCs drive extremely large air–sea CO_2 fluxes *instantaneously* – during their passage – due to high wind speeds, thereby enhancing ocean outgassing (Fig. 2A,B, Fig. S2A,B). These fluxes are up to 20–40 times larger than CO_2 fluxes during non-TC conditions (1–31 October), in line with observations and previous regional modeling work [13, 14, 16]. The largest instantaneous CO_2 fluxes occur within a radius of 150-200 kilometers from the TC center at their full development, where wind speeds are the strongest (Fig. 1E-F, Fig. S3).

Second, our TCs cause a *longer-lasting* effect driven by sea surface cooling. The TC-driven rapid decrease in sea surface temperature (SST) causes an also rapid decrease pCO_2 that persists after their passage (Fig. 2C-F), in line with observations and regional modeling work [e.g. 13, 43]. The link between decreasing SST and CO_2 flux anomalies is visible in the wake of TC1 (Fig . 1F,G). The cool and low-pCO_2 wake is shifted to the right of the TC track, which is a characteristic feature of fast-translating TCs [21, 24]. The rightward shift is explained by the fact that TC wind vectors rotate in phase with the inertial current vectors to the right of the TC track [20, 44].

Sea surface cooling reduces surface ocean pCO_2 by $\sim$10-40 ppm after each TC in the extra-tropics (Fig. 2F, Fig. S4, see *'Decomposing changes in pCO_2'* in Methods). The cooling impact on decreasing surface pCO_2 is only slightly counterbalanced by entrainment of dissolved inorganic carbon (DIC), and by increasing surface salinity, both increasing surface pCO_2, especially at latitudes north of 35°N (Fig. S4B,C). The latter is explained by vertical diffusion of salinity, which dominates over freshening due to surface fluxes (precipitation $>$ evaporation during both TCs). The relative role of temperature, DIC and salinity in changing surface pCO_2 in response to TCs varies substantially

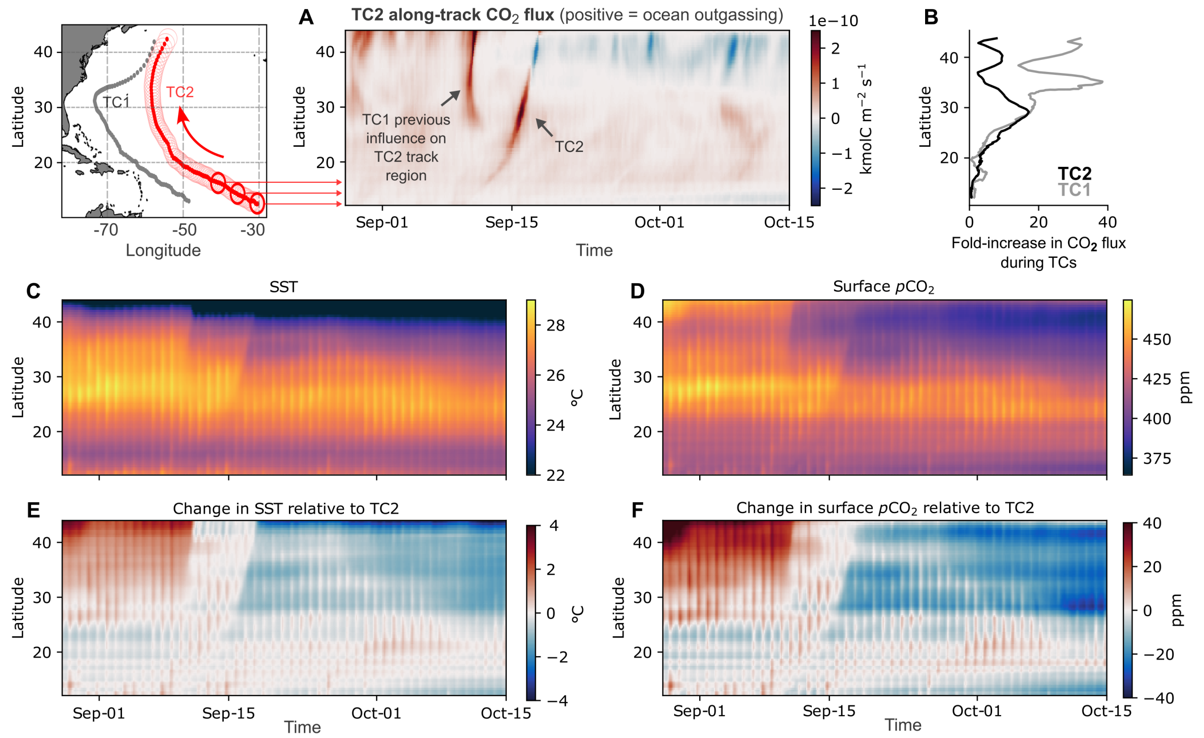

Figure 2: **Along-track time-series diagrams of TC2 impacts on CO_2.** Time series averaged over a moving 200 km-radius circle around the center of TC2 along its track. Shown quantities are air-sea CO_2 fluxes (**A**, negative indicates ocean uptake), and the fold-increase in air-sea CO_2 flux during the passage of the TCs along their tracks in comparison to 1-31 October, when no other TCs have occurred in this region (**B**). TC2 along-track absolute values of surface ocean pCO_2 (**C**), sea-surface temperature (SST, **D**), and their changes with respect to 12 hours before the TC2 passage (**E** and **F**, respectively). The vertical axes show the latitude coordinates of the center of TC2 along its track. The two-step reduction in pCO_2 and SST one followed 5-6 days after the other, shows the overlapping impacts of TC1 on the track of TC2 especially above 30°N. One can also see the daily cycle in the background as vertical stripes in all time-series diagrams. TC1 along-track time-series diagram for CO_2 is shown in Fig S2.

in different regions and between individual TC episodes [e.g. 16–19, 43, 45]. In the North Carolina estuary, for example, TCs have been observed to cause net CO_2 outgassing, where increasing surface DIC outweighs the cooling effect [46–48]. Pre-existing gradients in temperature, DIC, alkalinity and salinity, as well as cyclone intensity and translation speed, and thus their ability to induce vertical mixing, will altogether determine their net effect on pCO_2 anomalies [49, 50].

The CO_2 flux response to the longer-lasting cooling effect depends on the resulting local imbalance in pCO_2 between the surface ocean and atmosphere. The western North Atlantic is supersaturated in pCO_2 before the arrival of our TCs (i.e. ${pCO_2}^{ocean} > {pCO_2}^{atmosphere}$), which causes them to induce ocean CO_2 outgassing during their passage. Reducing surface pCO_2 either decreases ocean CO_2 outgassing, or induces uptake if the pCO_2 imbalance is inverted to undersaturated conditions (i.e. ${pCO_2}^{ocean} < {pCO_2}^{atmosphere}$).

Accumulating CO_2 fluxes from 24 hours preceding the TCs reveals that the longer-lasting cooling effect outweighs the instantaneous outgassing by mid September, especially after TC2 and at latitudes higher than 30°N, resulting in a net increase in ocean CO_2 uptake (Fig. S1C). The opposing instantaneous and longer-lasting TC impacts on air-sea CO_2 fluxes have been suggested to nearly cancel each other out at the global and annual scales, as well as regionally in the North Atlantic [15]. In other tropical regions, this effect may be less well-balanced. Previous work performed with a global ocean model forced by atmospheric reanalyses showed that TCs would cause net ocean CO_2 outgassing in the eastern North Pacific, but net uptake in the western North Pacific, and account for 2% and 33% of the net CO_2 flux regionally, respectively [15].

Considering only their instantaneous effect, our two TCs together induce about 0.9 TgC in CO_2 outgassing (1 TgC = 10^{12}g or 1 million metric tons of carbon) during their passage (integrated over a 200 km-radius circle along their tracks). This is equivalent to $\sim$18% of the outgassing that takes place in their track region during the warm season (July-September, $+5.1$ TgC), while also equivalent to less than 2% of the CO_2 uptake that takes place in the same region over the rest of the year (-63.8 TgC). While it is straightforward to quantify the instantaneous outgassing impact of our TCs by integrating CO_2 fluxes in their track region during their passage, quantifying their longer-lasting cooling impact in isolation is sensitive to the integration time window once chooses. Instead, here we underline that our TCs contribute to inverting the air-sea CO_2 flux direction – from ocean CO_2 outgassing to uptake – by modulating surface pCO_2 variability that has remained so far unresolved in global coupled ESMs.

2.2 Hurricanes trigger second phytoplankton bloom in autumn

We simulate a local increase in net primary production (NPP) by 1-2 orders of magnitude in response to our TCs (Fig. 3A), in agreement with satellite observations [25–27]. Similarly to the cooling effect, the NPP increase is also shifted to the right of the TC tracks, according to theory and observations [20, 52], which is especially true for fast-translating TCs [25, 39]. However, the TC-driven increase in phytoplankton concentration is not spatially restricted to the vicinity of their tracks. The Gulf Stream and its mesoscale meanders play an important role in transporting phytoplankton away from the track of TC1 after its passage (Fig. 3B-C). In fact, TCs themselves also intensify surface currents [53, 54], contributing to further spread their biological impact. The spatial spread of phytoplankton is mainly done by geostrophic currents, which are characterized by flowing along contours of sea-surface height anomalies (Fig. 3B-C). This highlights the role of the pronounced mesoscale, high eddy kinetic energy currents in advecting phytoplankton horizontally away from the TC track, which continues for several days after the TC passage. Therefore, the increase in phytoplankton concentration in the wake of TCs is thus partly counterbalanced by horizontal advection (Fig. S5A-C). Consequently, our simulated TCs trigger a phytoplankton bloom that spreads across the western North Atlantic far beyond the region of hurricane-force winds.

Our simulated TCs contribute to the development of a phytoplankton bloom in autumn, distinct from the spring bloom (Fig. 3D). The observed seasonal cycle of chlorophyll-a in the western North Atlantic shows a peak in spring, a minimum by the end of summer, and a growing phase during autumn (Fig. 3E). Although our simulation does not yet perfectly reproduce the observed phytoplankton phenology, it represents an improvement compared to state-of-the-art ESMs, in that our TCs trigger a phytoplankton bloom in autumn. ESMs are able to represent the spring bloom from observations, but they generally fail to capture the autumn recovery (Fig. 3F). A realistic representation of phytoplankton phenology by ESMs has been a long-lasting challenge, especially in capturing such secondary blooms in mid latitudes [55]. The occurrence of distinct autumn blooms is observed along the North Atlantic current further north at 40-50°N [56], generally triggered by mixed-layer deepening by storms, not necessarily only TCs [57–59]. Nevertheless, the role of TCs in triggering autumn blooms has been reported in observations [25, 39, 60], and TCs are suggested to drive interannual variability of chlorophyll-a in the western North Atlantic [25, 57]. In 2020, hurricanes Paulette and Teddy followed paths similar

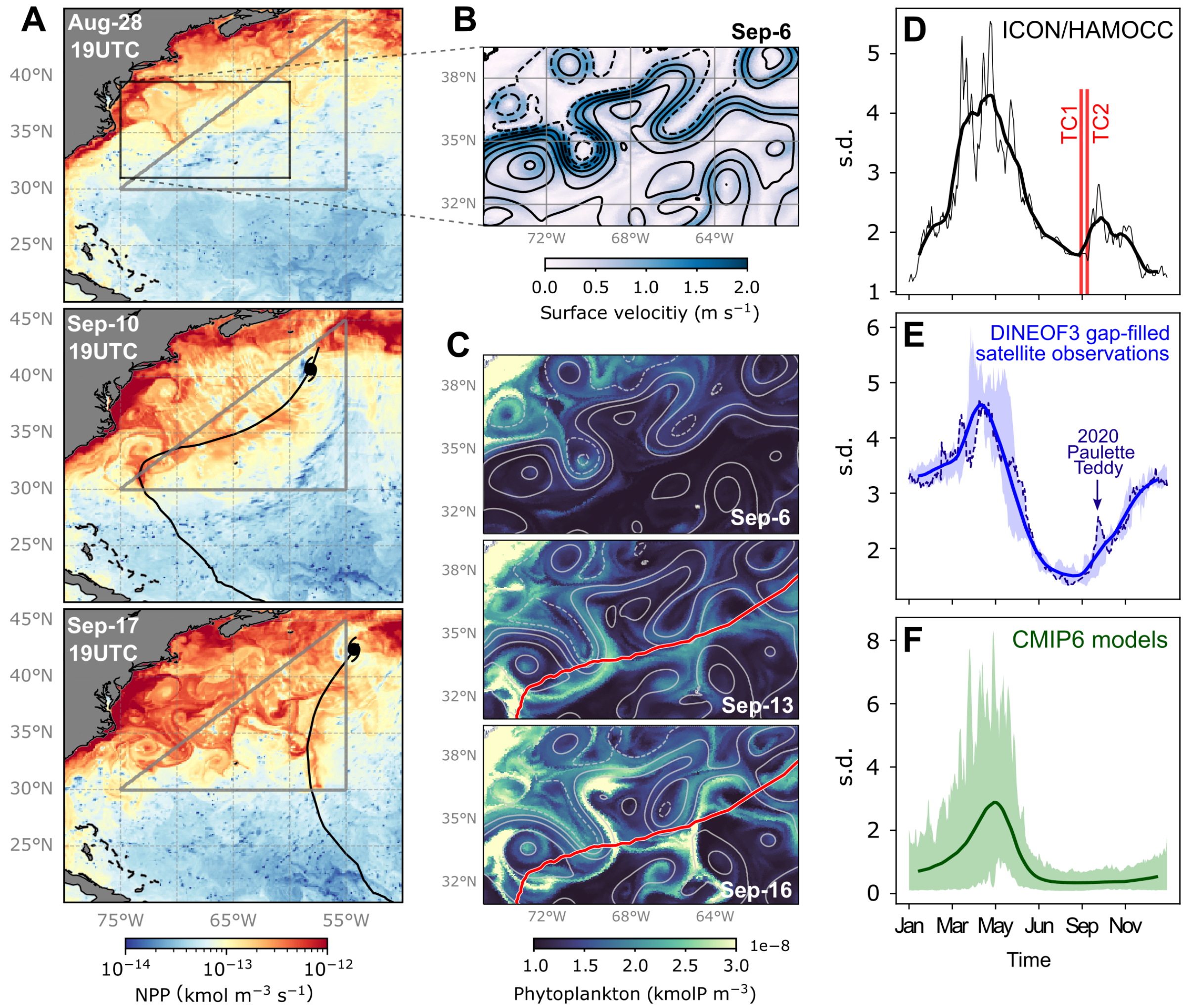

Figure 3: **Growth and spread of phytoplankton in response to TCs. A)** Vertically integrated net primary production (NPP) on 28 August 2020 (upper panel, before the hurricanes), on 10 September 2020 (middle panel, after TC1), and on 17 September (lower panel, after TC2). **B)** Zoomed-in map of surface velocities and sea-surface height anomalies (contours) in the Gulf Stream box shown in A. **C)** Temporal evolution of vertically integrated phytoplankton in the Gulf Stream box on 6 September (upper panel, before TC1), on 13 (middle panel) and 16 September (lower panel) after TC1, whose track is shown in red. **D)** Time series of Chlorophyll-a concentrations averaged over the western North Atlantic (triangle in A) in our 1-year ICON simulation, **E)** from satellite observations in 2018-2022, and **F)** in a CMIP6 multi-model mean in 2010-2014. CMIP6 models with daily chlorophyll data available are MPI-ESM-LR (HAMOCC), IPSL-CM6A-LR (NEMO-PISCES), and CESM2 (MARBL). Chlorophyll-a data in E are obtained from NOAA CoastWatch at coastwatch.noaa.gov/cwn/index.html, which are derived from multiple satellites (VIIRS-SNPP, VIIRS-NOAA-20, and OLCI-Sentinel-3A) and processed with the DINEOF gap-filling method [51]. Thin lines in D-F show daily data, while thick line are a 31-day running mean.

to those of our simulated TCs, and triggered a September peak in phytoplankton concentrations in the western North Atlantic (Fig. 3E, Fig S6). By resolving the km-scale interactions between atmosphere and ocean biogeochemistry, we also increase the realism of the biological response to intense TCs.

2.3 Cascading physical-biogeochemical response to hurricanes

Our TCs induce a sudden decrease in upper-ocean stratification, thereby increasing the mixed-layer depth by 20-40 m at their maximum intensity (Fig. 4A,B, Fig. S7A). Strong surface wind speeds also induce an instantaneous pulse of nutrient entrainment into the euphotic zone by turbulent mixing (Fig. S8A,B). While NPP responds immediately to the presence of nutrients (Fig. 3A), maxima in phytoplankton concentration occur days to weeks later (Fig. 4C, Fig. S5A). Phytoplankton is continuously diffused from the upper layers downwards by wind-driven mixing (Fig S8D, Fig. S9A,B). The vertical diffusion and advection of phytoplankton is mostly contained within the upper 100 meters in the wake of TCs (Fig. S5D,E).

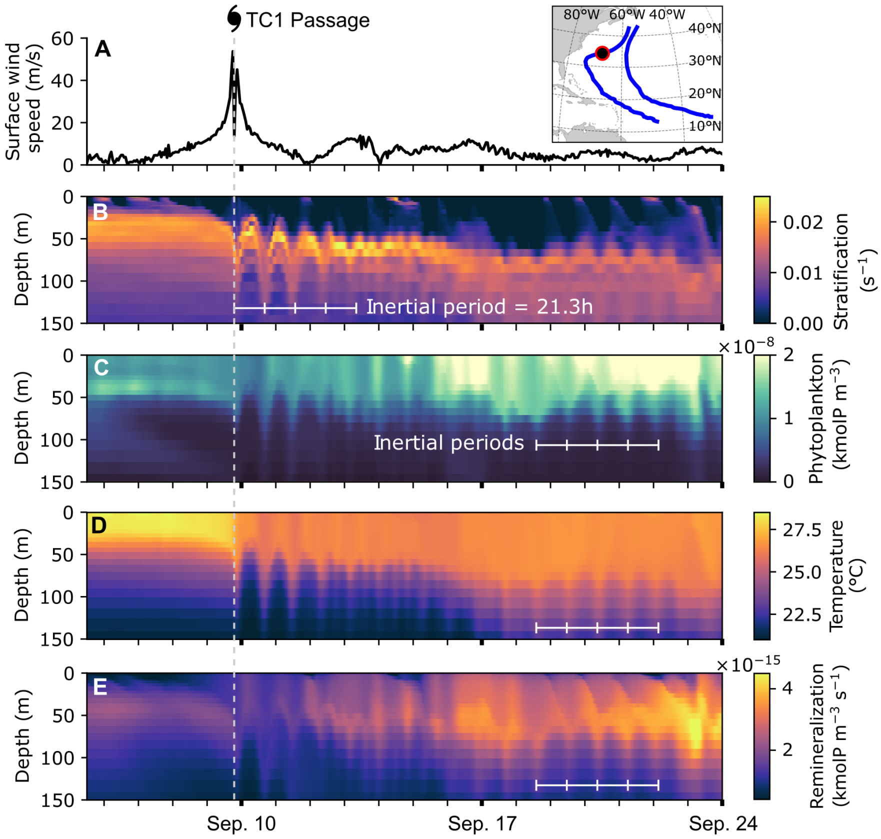

Figure 4: **Cascading physical and biogeochemical response to hurricane passage.** Time series from a fixed point in space (about 37°N and 67°W, see inset map) on the track of TC1, depicting conditions from before and after its passage as a category 4 hurricane. Variables shown are surface wind speed **(A)**, and vertical profiles of density stratification expressed as the Brunt-Väisälä frequency **(B)**, phytoplankton concentration **(C)**, temperature **(D)**, and aerobic organic matter remineralization **(E)**. Small white axes indicate the local inertial period at this latitude.

Near-inertial oscillations are triggered by the TCs, and become the prevailing mode of variability in the surface and subsurface ocean in their wake region, propagating horizontally and vertically downwards [20]. The horizontal advection of phytoplankton takes place mostly at near-inertial frequencies (Fig. S8C, Fig. S9C), which underscores their role in spatially spreading the TC-driven bloom. The downward propagation of near-inertial waves also transport kinetic energy [52] and further mix the thermocline, thus contributing to sustaining subsurface warming for weeks after the TC passage (Fig. 4D) [61, 62]. The surface cooling and subsurface warming – a typical dichotomy in the wake of TCs [20, 63] – is reproduced in our simulations, where 50m-temperatures increase by 1-1.5°C in the wake of TCs (Fig. S7B).

Our simulated TC-driven subsurface warming contributes to enhance organic matter remineralization (Fig. 4D-E), in addition to the increase in biological production itself. Increasing remineralization, in turn, decreases the amount of carbon exported to depth. The impact of TCs on increasing organic matter export is, therefore, not as pronounced as their impact organic matter production by phytoplankton (Fig. S10A). Only about 8-10% of the organic matter produced in the euphotic zone is exported to depths below 100 m in the western North Atlantic in our simulation (Fig. S10B). We do not detect a peak in export ratios in response to our TCs passage, as opposed to recent observations [30]. Nevertheless, our export ratios compare well with osbervations-based estimates near Bermuda (6.3-8.4% at 150m [64]). In the western North Atlantic, export ratio estimates range at least between 5-30%, with values generally increasing form the open ocean towards coastal zones (see [65, 66] and references therein).

3 Conclusion

We have conducted the first storm- and eddy-resolving (5 km ocean, 5 km atmosphere) global coupled ESM simulation including ocean biogeochemistry, which allowed us to resolve atmosphere-ocean biogeochemistry interactions in the km-scale within the Earth system for the first time. We have investigated two particularly intense TCs reaching category-4 hurricane force (surface wind speed >58 m/s) in the North Atlantic, which state-of-the-art ESMs have been, so far, unable to capture.

We have resolved the cascade of physical-biogeochemical effects that unfold in response to TCs in a global coupled ESM the first time. Extreme wind speeds enhance CO_2 outgassing by 20-40 times from the western North Atlantic, initially supersaturated in pCO_2. Our TCs also cool the surface ocean by 1-2°C each, decreasing the surface ocean pCO_2 by 10-40 ppm to undersaturated levels. Upwelling and mixing of DIC only slightly counteract the cooling effect on surface pCO_2. Consequently, our TCs contribute to inverting the CO_2 flux direction from ocean outgassing to ocean uptake. Moreover, our intense TCs increase NPP locally by 10-100 times, triggering a phytoplankton bloom in autumn, which typical ESMs so far fail to represent. This distinct autumn bloom persists in the western North Atlantic for weeks after the TC passage. Phytoplankton is spread horizontally by ocean mesoscale currents, especially in the vicinity of the Gulf Stream. TC-driven subsurface warming increases organic matter remineralization, thus impeding a larger impact of the TC-driven bloom on organic carbon export to depth.

The frequency and intensity of extreme weather events increase in response to climate change. The proportion of intense TCs is projected to increase in the future with *"high confidence"* according to the latest IPCC report [4], and so is their impact on the ocean carbon cycle. TCs intensify particularly fast in response to marine heatwaves [67, 68], which will also tend to become more intense in the future [69, 70]. The large variability between TCs, and extreme events overall, prevents generalizations of our findings in time or space, for which longer simulations are needed. Longer km-scale ESM simulations (with grid-spacing of 5 km or finer) are necessary to realistically represent such future changes, their impacts and feedbacks to climate by modulating the ocean CO_2 sink. Our work shows that this is now possible. By resolving small-scale interactions between atmosphere and ocean biogeochemistry in a global coupled ESM, we bridge the gap between km-scale mechanisms and the ocean carbon cycle at global and climatic scales.

Acknowledgements

DMN and TI are funded by the *Deutsche Forschungsgemeinschaft* (DFG, German Research Foundation) under Germany's Excellence Strategy – EXC 2037 'CLICCS - Climate, Climatic Change, and Society' – Project Number: 390683824, contribution to the Center for Earth System Research and Sustainability (CEN) of Universität Hamburg, and the Max Planck Institute of Meteorology. TI is funded by the EU Horizon 2020 research and innovation program under grant agreement 101003536 (project ESM2025–Earth System Models for the Future). FC is funded by BMBF (Federal Ministry of Education and Research) under IFCES2 project with grant number 16ME0692 as part of the SCALEXA funding guideline, which in turn was funded by the European Union - NextGenerationEU. AK is funded by the EU Horizon 2020 grant agreement 101003470 (nextGEMS project). Computational resources were provided by the German Climate Computing Center (DKRZ). We thank Lennart Ramme for his valuable feedback on the manuscript.

Author Contributions

TI and CH conceived the project "Coupled Climate Carbon Cycle Sapphire (C4S)". DMN, FC, NS and TI conceived this study's idea. FC developed the coupled ICON model configuration with HAMOCC. DMN conducted the ocean-only spinup, and FC conducted the coupled ICON experiments. FC, NS and NB implemented the online calculation of budget terms. AK implemented the tracking algorithm and characterized the tropical cyclones. DMN analyzed the model output with support from all authors. DMN wrote the manuscript, revised by all authors.

Competing Interests

The authors declare no competing interests.

References

1. Friedlingstein, P. *et al.* Global Carbon Budget 2023. *Earth System Science Data* **15,** 5301–5369. doi:10.5194/essd-15-5301-2023 (2023).
2. Gruber, N. *et al.* Trends and variability in the ocean carbon sink. *Nature Reviews Earth & Environment* **4,** 119–134. ISSN: 2662-138X. doi:10.1038/s43017-022-00381-x (2023).
3. Eyring, V. *et al.* Overview of the Coupled Model Intercomparison Project Phase 6 (CMIP6) experimental design and organization. *Geoscientific Model Development* **9,** 1937–1958. doi:10.5194/gmd-9-1937-2016 (2016).
4. Seneviratne, S. *et al.* in *Climate Change 2021: The Physical Science Basis. Contribution of Working Group I to the Sixth Assessment Report of the Intergovernmental Panel on Climate Change* (eds Masson-Delmotte, V. *et al.*) 1513–1766 (Cambridge University Press, Cambridge, United Kingdom and New York, NY, USA, 2021). doi:10.1017/9781009157896.013.
5. Murakami, H. & Sugi, M. Effect of Model Resolution on Tropical Cyclone Climate Projections. *SOLA* **6,** 73–76. doi:10.2151/sola.2010-019 (2010).
6. Davis, C. A. Resolving Tropical Cyclone Intensity in Models. *Geophysical Research Letters* **45,** 2082–2087. doi:10.1002/2017GL076966 (2018).

7. Haarsma, R. J. *et al.* High Resolution Model Intercomparison Project (HighResMIP v1.0) for CMIP6. *Geoscientific Model Development* **9,** 4185–4208. doi:`10.5194/gmd-9-4185-2016` (2016).

8. Roberts, M. J. *et al.* Projected Future Changes in Tropical Cyclones Using the CMIP6 HighResMIP Multimodel Ensemble. *Geophysical Research Letters* **47,** e2020GL088662. doi:`10.1029/2020GL088662` (2020).

9. Baker, A. J., Vannière, B. & Vidale, P. L. On the Realism of Tropical Cyclone Intensification in Global Storm-Resolving Climate Models. *Geophysical Research Letters* **51,** e2024GL109841. doi:`10.1029/2024GL109841` (2024).

10. Ilyina, T. *et al.* Global ocean biogeochemistry model HAMOCC: Model architecture and performance as component of the MPI-Earth system model in different CMIP5 experimental realizations. *Journal of Advances in Modeling Earth Systems* **5,** 287–315. doi:`10.1029/2012MS000178` (2013).

11. Hohenegger, C. *et al.* ICON-Sapphire: simulating the components of the Earth system and their interactions at kilometer and subkilometer scales. *Geoscientific Model Development* **16,** 779–811. doi:`10.5194/gmd-16-779-2023` (2023).

12. Kumar, A. U., Brüggemann, N., Smith, R. K. & Marotzke, J. Response of a tropical cyclone to a subsurface ocean eddy and the role of boundary layer dynamics. *Quarterly Journal of the Royal Meteorological Society* **148,** 378–402. doi:`10.1002/qj.4210` (2022).

13. Bates, N. R., Knap, A. H. & Michaels, A. F. Contribution of hurricanes to local and global estimates of air–sea exchange of CO2. *Nature* **395,** 58–61. doi:`10.1038/25703` (1998).

14. Perrie, W., Zhang, W., Ren, X., Long, Z. & Hare, J. The role of midlatitude storms on air-sea exchange of CO2. *Geophysical Research Letters* **31,** L09306. doi:`10.1029/2003GL019212` (2004).

15. Lévy, M. *et al.* Contribution of tropical cyclones to the air-sea CO2 flux: A global view. *Global Biogeochemical Cycles* **26,** GB2001. doi:`10.1029/2011GB004145` (2012).

16. Meng, Z., Guan, Y. & Feng, Y. Simulating the impact of typhoons on air-sea CO2 fluxes on the northern coastal area of the South China Sea. *Environmental Research Letters* **19,** 044008. doi:`10.1088/1748-9326/ad300e` (2024).

17. Li, D. *et al.* Hypoxic Bottom Waters as a Carbon Source to Atmosphere During a Typhoon Passage Over the East China Sea. *Geophysical Research Letters* **46,** 11329–11337. doi:`https://doi.org/10.1029/2019GL083933` (2019).

18. Nemoto, K. *et al.* Continuous observations of atmospheric and oceanic CO2 using a moored buoy in the East China Sea: Variations during the passage of typhoons. *Deep Sea Research Part II: Topical Studies in Oceanography* **56.** Surface Ocean CO2 Variability and Vulnerabilities, 542–553. ISSN: 0967-0645. doi:`10.1016/j.dsr2.2008.12.015` (2009).

19. Yu, P. *et al.* Effects of Typhoons on Surface Seawater pCO2 and Air-Sea CO2 Fluxes in the Northern South China Sea. *Journal of Geophysical Research: Oceans* **125,** e2020JC016258. doi:`10.1029/2020JC016258` (2020).

20. F.Price, J. Upper Ocean Response to a Hurricane. *Journal of Physical Oceanography* **11,** 153–175. doi:`10.1175/1520-0485(1981)011<0153:UORTAH>2.0.CO;2` (1981).

21. Cheng, L., Zhu, J. & Sriver, R. L. Global representation of tropical cyclone-induced short-term ocean thermal changes using Argo data. *Ocean Science* **11,** 719–741. doi:10.5194/os-11-719-2015 (2015).

22. Takahashi, T., Olafsson, J., Goddard, J. G., Chipman, D. W. & Sutherland, S. C. Seasonal variation of CO_2 and nutrients in the high-latitude surface oceans: A comparative study. *Global Biogeochemical Cycles* **7,** 843–878. doi:10.1029/93GB02263 (1993).

23. Wanninkhof, R. Relationship between wind speed and gas exchange over the ocean revisited. *Limnology and Oceanography: Methods* **12,** 351–362. doi:10.4319/lom.2014.12.351 (2014).

24. Foltz, G. R., Balaguru, K. & Leung, L. R. A reassessment of the integrated impact of tropical cyclones on surface chlorophyll in the western subtropical North Atlantic. *Geophysical Research Letters* **42,** 1158–1164. doi:10.1002/2015GL063222 (2015).

25. Babin, S. M., Carton, J. A., Dickey, T. D. & Wiggert, J. D. Satellite evidence of hurricane-induced phytoplankton blooms in an oceanic desert. *Journal of Geophysical Research: Oceans* **109,** C03043. doi:10.1029/2003JC001938 (2004).

26. Lin, I. *et al.* New evidence for enhanced ocean primary production triggered by tropical cyclone. *Geophysical Research Letters* **30,** GL017141. doi:10.1029/2003GL017141 (2003).

27. Riyanka Roy Chowdhury, S. P. K. & Chakraborty, A. A study on the physical and biogeochemical responses of the Bay of Bengal due to cyclone Madi. *Journal of Operational Oceanography* **15,** 104–125. doi:10.1080/1755876X.2020.1817659 (2022).

28. Siswanto, E., Morimoto, A. & Kojima, S. Enhancement of phytoplankton primary productivity in the southern East China Sea following episodic typhoon passage. *Geophysical Research Letters* **36,** L11603. doi:10.1029/2009GL037883 (2009).

29. Wang, Y. Composite of Typhoon-Induced Sea Surface Temperature and Chlorophyll-a Responses in the South China Sea. *Journal of Geophysical Research: Oceans* **125,** e2020JC016243. doi:10.1029/2020JC016243 (2020).

30. Pedrosa-Pàmies, R., Conte, M. H., Weber, J. C. & Johnson, R. Hurricanes Enhance Labile Carbon Export to the Deep Ocean. *Geophysical Research Letters* **46,** 10484–10494. doi:10.1029/2019GL083719 (2019).

31. Ye, S., Zhang, R.-H., Wang, H., Tian, F. & Shi, Q. Tropical Cyclone-Induced Ecological Responses and Their Feedback on Physical Fields: A Case Study for Hurricane Fernanda (2017). *Journal of Geophysical Research: Oceans* **129,** e2024JC021150. doi:10.1029/2024JC021150 (2024).

32. Kim, H.-K. *et al.* Western North Pacific tropical cyclone activity modulated by phytoplankton feedback under global warming. *Nature Climate Change* **14,** 504–510. doi:10.1038/s41558-024-01976-6 (2024).

33. Johnston, T. M. S., Rudnick, D. L., Brizuela, N. & Moum, J. N. Advection by the North Equatorial Current of a Cold Wake due to Multiple Typhoons in the Western Pacific: Measurements From a Profiling Float Array. *Journal of Geophysical Research: Oceans* **125,** e2019JC015534. doi:10.1029/2019JC015534 (2020).

34. De Moeland Andrew B. Martinezand Sanne Muisand Ivan D. Haighand Karin van der Wieland Reindert J. Haarsmaand Philip J. Wardand Malcolm J. Robertsand Job C. M. Dullaartand Jeroen C. J. H. Aerts, N. B. H. A globally consistent local-scale assessment of future tropical cyclone risk. *Science Advances* **8,** eabm8438. doi:10.1126/sciadv.abm8438 (2022).

35. Knutson, T. R. & Tuleya, R. E. Impact of CO2-Induced Warming on Simulated Hurricane Intensity and Precipitation: Sensitivity to the Choice of Climate Model and Convective Parameterization. *Journal of Climate* **17,** 3477–3495. doi:10.1175/1520-0442(2004)017<3477:IOCWOS>2.0.CO;2 (2004).

36. Emanuel, K. A. Downscaling CMIP5 climate models shows increased tropical cyclone activity over the 21st century. *Proceedings of the National Academy of Sciences* **110,** 12219–12224. doi:10.1073/pnas.1301293110 (2013).

37. National Hurricane Center and Central Pacific Hurricane Center, National Oceanographic and Atmospheric Administration (NOAA). *Hurricane Paulette (2020)* https://www.nhc.noaa.gov/archive/2020/PAULETTE_graphics.php. Accessed: 3 December 2024. 2020.

38. Ma, Z., Yan, X. & Fei, J. Quantifying the Rightward Bias Extent of Tropical Cyclones' Cold Wakes. *Geophysical Research Letters* **50,** e2023GL104578. doi:10.1029/2023GL104578 (2023).

39. Lin, I.-I. Typhoon-induced phytoplankton blooms and primary productivity increase in the western North Pacific subtropical ocean. *Journal of Geophysical Research: Oceans* **117,** C03039. doi:10.1029/2011JC007626 (2012).

40. Cione, J. J., Black, P. G. & Houston, S. H. Surface Observations in the Hurricane Environment. *Monthly Weather Review* **128,** 1550–1561. doi:10.1175/1520-0493(2000)128<1550:SOITHE>2.0.CO;2 (2000).

41. De Abreu Sá, L. D., Viswanadham, Y. & Manzi, A. O. Energy flux partitioning over the Amazon forest. *Theoretical and Applied Climatology* **39,** 1–16. doi:10.1007/BF00867653 (1988).

42. Hasler, N. & Avissar, R. What Controls Evapotranspiration in the Amazon Basin? *Journal of Hydrometeorology* **8,** 380–395. doi:10.1175/JHM587.1 (2007).

43. Huang, P. & Imberger, J. Variation of pCO2 in ocean surface water in response to the passage of a hurricane. *Journal of Geophysical Research: Oceans* **115,** C10024. doi:10.1029/2010JC006185 (2010).

44. Samson, G., Giordani, H., Caniaux, G. & Roux, F. Numerical investigation of an oceanic resonant regime induced by hurricane winds. *Ocean Dynamics* **59,** 565–586. ISSN: 1616-7228. doi:10.1007/s10236-009-0203-8 (2009).

45. Bhattacharya, T., Chakraborty, K., Ghoshal, P. K., Ghosh, J. & Baduru, B. Response of Surface Ocean pCO2 to Tropical Cyclones in Two Contrasting Basins of the Northern Indian Ocean. *Journal of Geophysical Research: Oceans* **128,** e2022JC019058. doi:10.1029/2022JC019058 (2023).

46. Crosswell, J. R., Wetz, M. S., Hales, B. & Paerl, H. W. Extensive CO2 emissions from shallow coastal waters during passage of Hurricane Irene (August 2011) over the Mid-Atlantic Coast of the U.S.A. *Limnology and Oceanography* **59,** 1651–1665. doi:10.4319/lo.2014.59.5.1651 (2014).

47. Van Dam, B. R., Crosswell, J. R. & Paerl, H. W. Flood-driven CO2 emissions from adjacent North Carolina estuaries during Hurricane Joaquin (2015). *Marine Chemistry* **207,** 1–12. ISSN: 0304-4203. doi:10.1016/j.marchem.2018.10.001 (2018).

48. Osburn, C. L., Rudolph, J. C., Paerl, H. W., Hounshell, A. G. & Van Dam, B. R. Lingering Carbon Cycle Effects of Hurricane Matthew in North Carolina's Coastal Waters. *Geophysical Research Letters* **46,** 2654–2661. doi:10.1029/2019GL082014 (2019).

49. Mahadevan, A. *et al.* Impact of episodic vertical fluxes on sea surface pCO_2. *Philosophical Transactions of the Royal Society A: Mathematical, Physical and Engineering Sciences* **369,** 2009–2025. doi:10.1098/rsta.2010.0340 (2011).

50. Ye, H. *et al.* Variation of pCO2 concentrations induced by tropical cyclones "Wind-Pump" in the middle-latitude surface oceans: A comparative study. *PLOS ONE* **15,** 1–20. doi:10.1371/journal.pone.0226189 (2020).

51. Liu, X. & Wang, M. Global daily gap-free ocean color products from multi-satellite measurements. *International Journal of Applied Earth Observation and Geoinformation* **108,** 102714. ISSN: 1569-8432. doi:https://doi.org/10.1016/j.jag.2022.102714 (2022).

52. Pallàs-Sanz, E., Candela, J., Sheinbaum, J. & Ochoa, J. Mooring observations of the near-inertial wave wake of Hurricane Ida (2009). *Dynamics of Atmospheres and Oceans* **76.** The Loop Current Dynamics Experiment, 325–344. ISSN: 0377-0265. doi:10.1016/j.dynatmoce.2016.05.003 (2016).

53. Sun, L. *et al.* Effects of super typhoons on cyclonic ocean eddies in the western North Pacific: A satellite data-based evaluation between 2000 and 2008. *Journal of Geophysical Research: Oceans* **119,** 5585–5598. doi:10.1002/2013JC009575 (2014).

54. Lu, Z., Wang, G. & Shang, X. Response of a Preexisting Cyclonic Ocean Eddy to a Typhoon. *Journal of Physical Oceanography* **46,** 2403–2410. doi:10.1175/JPO-D-16-0040.1 (2016).

55. Kostadinov, T. S. *et al.* Inter-comparison of phytoplankton functional type phenology metrics derived from ocean color algorithms and Earth System Models. *Remote Sensing of Environment* **190,** 162–177. ISSN: 0034-4257. doi:10.1016/j.rse.2016.11.014 (2017).

56. González Taboada, F. & Anadón, R. Seasonality of North Atlantic phytoplankton from space: impact of environmental forcing on a changing phenology (1998–2012). *Global Change Biology* **20,** 698–712. doi:10.1111/gcb.12352 (2014).

57. Martinez, E., Antoine, D., D'Ortenzio, F. & de Boyer Montégut, C. Phytoplankton spring and fall blooms in the North Atlantic in the 1980s and 2000s. *Journal of Geophysical Research: Oceans* **116,** C11029. doi:10.1029/2010JC006836 (2011).

58. Lévy, M. *et al.* Production regimes in the northeast Atlantic: A study based on Sea-viewing Wide Field-of-view Sensor (SeaWiFS) chlorophyll and ocean general circulation model mixed layer depth. *Journal of Geophysical Research: Oceans* **110,** C07S10. doi:10.1029/2004JC002771 (2005).

59. Painter, S. C., Finlay, M., Hemsley, V. S. & Martin, A. P. Seasonality, phytoplankton succession and the biogeochemical impacts of an autumn storm in the northeast Atlantic Ocean. *Progress in Oceanography* **142,** 72–104. ISSN: 0079-6611. doi:10.1016/j.pocean.2016.02.001 (2016).

60. Ye, H. *et al.* Storm-induced changes in pCO2 at the sea surface over the northern South China Sea during Typhoon Wutip. *Journal of Geophysical Research: Oceans* **122,** 4761–4778. doi:10.1002/2016JC012643 (2017).

61. Moum, N. G. B. M. H. A. S.-P. X. J. S. G. V. S. J. W. K. H. J. N. Prolonged thermocline warming by near-inertial internal waves in the wakes of tropical cyclones. *Proceedings of the National Academy of Sciences* **120,** e2301664120. doi:10.1073/pnas.2301664120 (2023).

62. Bond, N. A. *et al.* Upper ocean response to Typhoon Choi-Wan as measured by the Kuroshio Extension Observatory mooring. *Journal of Geophysical Research: Oceans* **116,** C02031. doi:10.1029/2010JC006548 (2011).

63. Emanuel, K. Contribution of tropical cyclones to meridional heat transport by the oceans. *Journal of Geophysical Research: Atmospheres* **106,** 14771–14781. doi:10.1029/2000JD900641 (2001).

64. Conte, M., Pedrosa-Pamies, R., Weber, J. & Johnson, R. The climatology of the deep particle flux in the oligotrophic western North Atlantic gyre, 1978–2022. *Progress in Oceanography,* 103433. ISSN: 0079-6611. doi:10.1016/j.pocean.2025.103433 (2025).

65. Maerz, J., Six, K. D., Stemmler, I., Ahmerkamp, S. & Ilyina, T. Microstructure and composition of marine aggregates as co-determinants for vertical particulate organic carbon transfer in the global ocean. *Biogeosciences* **17,** 1765–1803. doi:10.5194/bg-17-1765-2020 (2020).

66. DeVries, T. & Weber, T. The export and fate of organic matter in the ocean: New constraints from combining satellite and oceanographic tracer observations. *Global Biogeochemical Cycles* **31,** 535–555. doi:10.1002/2016GB005551 (2017).

67. Radfar, S., Moftakhari, H. & Moradkhani, H. Rapid intensification of tropical cyclones in the Gulf of Mexico is more likely during marine heatwaves. *Communications Earth & Environment* **5,** 421. doi:10.1038/s43247-024-01578-2 (2024).

68. Choi, H.-Y., Park, M.-S., Kim, H.-S. & Lee, S. Marine heatwave events strengthen the intensity of tropical cyclones. *Communications Earth & Environment* **5,** 69. doi:10.1038/s43247-024-01239-4 (2024).

69. Frölicher, T. L., Fischer, E. M. & Gruber, N. Marine heatwaves under global warming. *Nature* **560,** 360–364. doi:10.1038/s41586-018-0383-9 (2018).

70. Barkhordarian, A., Nielsen, D. M. & Baehr, J. Recent marine heatwaves in the North Pacific warming pool can be attributed to rising atmospheric levels of greenhouse gases. *Communications Earth & Environment* **3,** 131. doi:10.1038/s43247-022-00461-2 (2022).

Methods

ICON model and simulations

We use the ICOsahedral Non-hydrostatic (ICON) coupled model in the “Sapphire” configuration [11], which includes atmospheric, ocean, land and ocean biogeochemistry components. ICON uses a unstructured triangular grid, here configured with nominal mean horizontal resolution of 5 km in all components. The atmospheric dynamics are based on the numerical weather prediction (NWP) model by the German Weather Service (DWD) [71]. In the atmosphere, convection is explicitly resolved, while parameterizations are only used in processes that cannot be resolved in the km-scale, namely radiation, microphysics and turbulence [11]. The atmosphere is coupled to the ocean and sea-ice model ICON-O [72]. Here, ICON-O is configured with 72 layers in $z*$ coordinates, which distributes sea-surface height anomalies at every time step in all model layers. In our configuration, ICON-O resolves ocean eddies explicitly, and therefore parameterizations for eddy-induced horizontal diffusion and advection are switched off (i.e. GM-Redi [73, 74]), and only parameterizations for vertical turbulent mixing and dissipation are maintained [72]. Land biogeophysics and biogeochemistry are represented in JSBACH [75] version 4. Ocean biogeochmistry is included with the HAMburg Ocean Carbon Cycle (HAMOCC) model [10].

HAMOCC simulates biogeochemical processes in the water column, including interactions with the atmosphere and sediment. HAMOCC was initially developed based on a nutrient-phytoplankton-zooplankton-detritus (NPDZ) framework [76], but is now expanded to include the representation of 20 biogeochemical tracers [10]. Marine biology in HAMOCC is represented by two tracer variables: bulk phytoplankton, which includes calcifying and silicifying species, and cyanobacteria (diazotrophs) [77]. Phytoplankton growth is co-limited by nitrate, phosphate, and iron, while cyanobacteria can utilize dinitrogen. Our HAMOCC configuration includes the representation of dynamic particle sinking speeds in the water column through the M4AGO scheme [65], and temperature-dependent organic matter remineralization. A constant carbon-to-nutrient ratio is assumed for all marine organic matter following a global Redfield ratio concept [78]. HAMOCC is embedded in ICON-O, and therefore they share the same grid configuration.

Our coupled ICON configuration (ocean and atmosphere physics) is the same as that from Baker et al. [9], where they show that key TC characteristics are simulated realistically compared to observations, namely TC intensification rates, TC inner-core structure, and the relationship between TC size and intensification. Our ICON configuration only differs from that of Baker et al. in that we include the representation of ocean biogeochemistry with HAMOCC, and therefore also the feedback to the ocean physics through the dynamic representation of sunlight absorption by phytoplankton [79].

We use a step-wise strategy of model complexity and resolution to arrive at the initial conditions for our coupled model simulation. This strategy consists in initializing our model from previously tuned and spun-up simulations at coarser resolutions (Fig. 5), providing enough time for the next simulation to adapt to the given initial conditions. Our coupled simulation starts from a transient ocean 5 km ICON-O/HAMOCC simulation, and from the Integrated Forcast System (IFS) atmospheric analysis at 01-01-2020 [80]. The ocean biogeochemistry is taken from a well-tuned and well spun-up coarser ICON-O/HAMOCC simulation (40 km spatial resolution, 64 vertical layers) which, in turn, follows from a $>$3000 years-long ICON-O physics-only spin-up. The high-resolution ocean physics is taken from an ICON-O 5 km transient simulation started in 2010 forced with the ERA5 reanalysis [81] and increasing atmospheric CO_2 concentrations. We remap the 40 km HAMOCC variables onto the 5 km

ICON-O grid and run ICON-O with HAMOCC at 5 km from 01-01-2017 for three years to allow for enough time for the biogeochemical tracers in the upper ocean layers to adapt to the ocean mesoscale field. Spinning-up HAMOCC to reach quasi-stability in all layers and biogeochemical tracers, including in the ocean sediment, requires hundreds or thousands of years of simulations. Such long spin-ups are still impractical at 5 km resolution. The here-applied cascading strategy allows us to generate initial conditions with relatively stable conditions (sufficiently small drifts) in the euphotic zone – where we focus on in this study – and that are consistent with the ocean physics from the 5 km ocean model. Moreover, any long-term trends are small relative to the variability in our short 1-year simulation. After running the coupled model for one year with daily output, we repeat the simulation from 20-August to 31-October with hourly output.

TC tracking

We deploy a tracking algorithm that only requires 2D surface fields and closely follows the approach taken by Shimura et al. (2017) [82]. The algorithm takes the hourly mean sea-level pressure (MSLP) and near-surface wind speed over both land and ocean as inputs and consists of two main steps: (1) identifying candidate tropical cyclone points and (2) stitching together the points to create tracks. For each time step, we begin by finding the grid cell with the lowest MSLP. If the MSLP is less than 1010 hPa, the grid cell is stored as a candidate TC point and all grid cells within a 800 km radius are masked. This is repeated until the MSLP of all remaining grid cells exceeds 1010 hPa. In the second step, the tracks are formed by connecting candidate points with a surface wind speed of at least 17 m/s that are sufficiently close in time and space. To this end, we start by selecting the candidate point at the earliest possible time step within the region 0° N to 35° to mark the start of a track. We then look for the next candidate point to add to the track, which must lie within 100 km and the next 24 hours. Priority is given to points closer in time. In the case where multiple points are found for the same time step, the one with the lowest MSLP is selected and the remaining points are removed. The track is successively extended until no more candidate points satisfy the above conditions. This process is repeated until all candidate points are added to tracks or removed. In a further post-processing step, we retain only those tracks with a lifetime greater than 24 hours and lifetime maximum intensity that exceeds hurricane strength (>33 m/s).

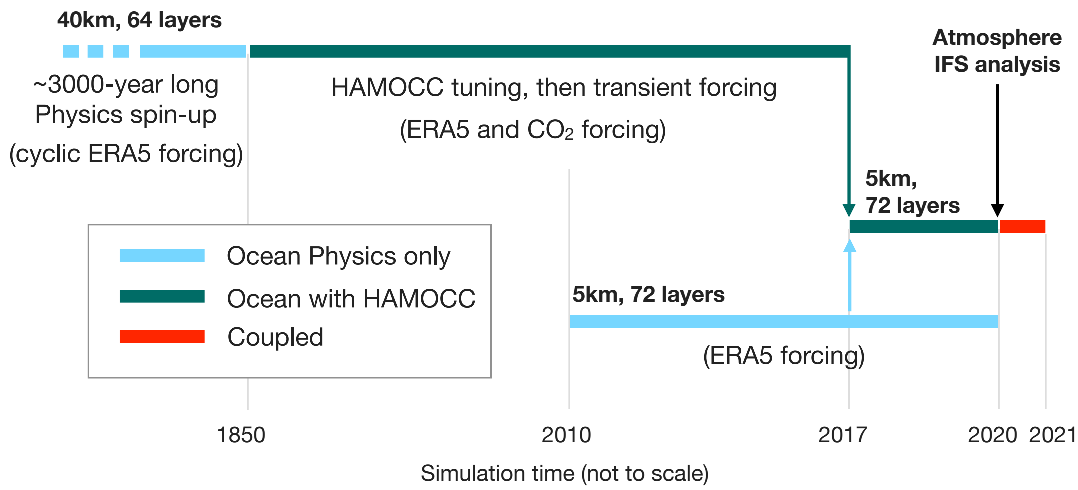

Figure 5: **Step-wise strategy for initialization.** Schematics of previous simulations performed for tuning and spin-up, leading to the initial conditions used for our coupled simulation.

Our algorithm identifies 42 TCs that reach at least category-1 hurricane intensity in our 1-year global simulation. We do not consider less intense tropical storms and depressions. Three of the 42 hurricane-force TCs take place in the North Atlantic. Here we focus on the two *intense* TCs (i.e. category 4 or higher), since they are those typically missed by ESMs. A third and weaker TC occurs in the Gulf of Mexico, reaching hurricane category 1 shortly before making landfall.

Ocean tracer budget terms

We explicitly calculate the contribution of each term composing the tendencies of most biogeochemical tracers, temperature, and salinity, during the ICON model integration. This tendency decomposition is calculated online at each time step, and stored as daily or hourly means, depending on the output frequency. The total tendency of tracer C is calculated as:

$$\frac{\partial C}{\partial t} = -\mathbf{U} \cdot \nabla C + \frac{\partial}{\partial z}\left(k_v \frac{\partial C}{\partial z}\right) + \text{Surface fluxes} + \text{Biogeochemical sources and sinks}, \quad (1)$$

where the terms on the right-hand-side are the contributions from advection (we calculate horizontal and vertical advection separately), vertical diffusion by turbulent mixing, and surface fluxes, respectively. $\mathbf{U} = (u, v, w)$ is the ocean velocity vector, and k_v is the vertical diffusion coefficient obtained using a turbulent kinetic energy (TKE) closure parameterization (see [72]).

The surface flux of CO_2 is calculated in HAMOCC as $F = k_w\ S_{CO_2}\ \left(pCO_2{}^{ocean} - pCO_2{}^{atmo}\right)$, where k_w is the gas transfer velocity, a function of temperature and the squared 10m wind speed, calculated according to [23], S_{CO_2} is the solubility of CO_2 in seawater, a function of temperature, calculated according to [83], $pCO_2{}^{ocean}$ is the surface ocean pCO_2 calculated at each time step from DIC and alkalinity concentrations, and $pCO_2{}^{atmo}$ is the surface atmospheric pCO_2 corrected for the total atmospheric pressure following the protocols for the Ocean Model Intercomparison Project (OMIP) [84]. In our simulation, atmospheric CO_2 concentrations are uniformly prescribed over the entire ocean surface following year 2020 values, and do not change in response to air-sea CO_2 fluxes.

Decomposing changes in pCO_2

Following Takahashi et al.[22], we decompose the total change in surface pCO_2 triggered by the passage of the TCs between contributions from changes in sea surface salinity (SSS), sea surface temperature (SST) and surface DIC and alkalinity concentrations:

$$\delta pCO_2^{Total} = \delta pCO_2^{SST} + \delta pCO_2^{SSS} + \delta pCO_2^{DIC} + \delta pCO_2^{Alk}. \quad (2)$$

Here "δ" denotes changes in time with respect to the TC passage, not to be confused with ΔpCO_2, which commonly represents the pCO_2 imbalance between ocean and atmosphere. Each term is calculated by scaling the simulated surface pCO_2 with changes in SST, SSS, DIC, and alkalinity:

$$\begin{aligned}
\delta pCO_2^{SST} &= \gamma_{SST}\ pCO_{2ref}\ \delta SST \\
\delta pCO_2^{SSS} &= \gamma_{SSS}\ pCO_{2ref}\ \delta SSS/SSS_{ref} \\
\delta pCO_2^{DIC} &= \gamma_{DIC}\ pCO_{2ref}\ \delta DIC/DIC_{ref} \\
\delta pCO_2^{Alk} &= \gamma_{Alk}\ pCO_{2ref}\ \delta Alk/Alk_{ref}
\end{aligned} \quad (3)$$

where "ref" denotes a local reference value taken 24 hours prior to the TC passage, $\gamma_{SST} = 0.0423°\text{C}^{-1}$, $\gamma_{SSS} = 1$ and, from our model data, we use the approximation presented by [85] to calculate:

$$\begin{aligned}\gamma_{DIC} &= \frac{3\ Alk\ DIC - 2\ DIC^2}{(2\ DIC - Alk)(Alk - DIC)} \\ \gamma_{Alk} &= \frac{Alk^2}{(2\ DIC - Alk)(Alk - DIC)}\end{aligned} \tag{4}$$

The coefficient γ_{DIC} – also known as the Revelle factor[86] – allows for a linear transformation between percentage changes in DIC and pCO_2, that is, a scaling factor between $\delta DIC/DIC_{ref}$ and $\delta pCO_2/pCO_{2ref}$. Similarly for γ_{Alk} and γ_{SSS}. On the other hand, γ_{SST} yields a 4.23% change in pCO_2 in response to a 1°C change in SST in absolute terms directly. Differences between the reconstructed δpCO_2^{Total} from Eq. 2 and its simulated value by ICON/HAMOCC are relatively small (Fig S4-E), which confirms the robustness of this widely-used method.

Data Availability

ICON output necessary to reproduce figures will be publicly available at the World Data Climate Center (WDCC) before this paper is accepted for publication.

Code Availability

Scripts used to reproduce figures will be made available at the Max Planck Society Publication Repository, before this paper is accepted for publication, at pure.mpg.de/pubman/faces/HomePage.jsp.

References

71. Zängl, G., Reinert, D., Rípodas, P. & Baldauf, M. The ICON (ICOsahedral Non-hydrostatic) modelling framework of DWD and MPI-M: Description of the non-hydrostatic dynamical core. *Quarterly Journal of the Royal Meteorological Society* **141,** 563–579. doi:`https://doi.org/10.1002/qj.2378` (2015).

72. Korn, P. *et al.* ICON-O: The Ocean Component of the ICON Earth System Model—Global Simulation Characteristics and Local Telescoping Capability. *Journal of Advances in Modeling Earth Systems* **14,** e2021MS002952. doi:`10.1029/2021MS002952` (2022).

73. Redi, M. H. Oceanic isopycnal mixing by coordinate rotation. *Journal of Physical Oceanography* **12,** 1154–1158. doi:`10.1175/1520-0485(1982)012<1154:OIMBCR>2.0.CO;2` (1982).

74. Gent, P. R. & Mcwilliams, J. C. Isopycnal Mixing in Ocean Circulation Models. *Journal of Physical Oceanography* **20,** 150–155. doi:`10.1175/1520-0485(1990)020<0150:IMIOCM>2.0.CO;2` (1990).

75. Reick, C. H. *et al.* The land component of the MPI Earth System Model: documentation of version 3.2. *Berichte zur Erdsystemforschung,* pp.271. doi:`10.17617/2.3279802` (2021).

76. Six, K. D. & Maier-Reimer, E. Effects of plankton dynamics on seasonal carbon fluxes in an ocean general circulation model. *Global Biogeochemical Cycles* **10,** 559–583. doi:`https://doi.org/10.1029/96GB02561` (1996).

77. Paulsen, H., Ilyina, T., Six, K. D. & Stemmler, I. Incorporating a prognostic representation of marine nitrogen fixers into the global ocean biogeochemical model HAMOCC. *Journal of Advances in Modeling Earth Systems* **9,** 438–464. doi:10.1002/2016MS000737 (2017).

78. Redfield, A. On the proportions of organic derivatives in seawater and their relation to the composition of plankton. *James Johnstone Memorial Volume,* 176–192 (1934).

79. Wetzel, P. *et al.* Effects of Ocean Biology on the Penetrative Radiation in a Coupled Climate Model. *Journal of Climate* **19,** 3973–3987. doi:10.1175/JCLI3828.1 (2006).

80. ECMWF. *Integrated Forecasting System (IFS)* https://www.ecmwf.int/en/forecasts/documentation-and-support/changes-ecmwf-model. Accessed on 2022-02-20. 2022.

81. Hersbach, H. *et al.* The ERA5 global reanalysis. *Quarterly Journal of the Royal Meteorological Society* **146,** 1999–2049. doi:https://doi.org/10.1002/qj.3803 (2020).

82. Shimura, T., Mori, N. & Hemer, M. A. Projection of tropical cyclone-generated extreme wave climate based on CMIP5 multi-model ensemble in the Western North Pacific. *Climate Dynamics* **49,** 1449–1462. ISSN: 14320894. doi:10.1007/s00382-016-3390-2 (4 Aug. 2017).

83. Weiss, R. Carbon dioxide in water and seawater: the solubility of a non-ideal gas. *Marine Chemistry* **2,** 203–215. ISSN: 0304-4203. doi:10.1016/0304-4203(74)90015-2 (1974).

84. Orr, J. C. *et al.* Biogeochemical protocols and diagnostics for the CMIP6 Ocean Model Intercomparison Project (OMIP). *Geoscientific Model Development* **10,** 2169–2199. doi:10.5194/gmd-10-2169-2017 (2017).

85. Sarmiento, J. L. & Gruber, N. *Ocean Biogeochemical Dynamics* ISBN: 9780691017075. doi:10.2307/j.ctt3fgxqx (Princeton University Press, 2006).

86. Revelle, R. & Suess, H. E. Carbon Dioxide Exchange Between Atmosphere and Ocean and the Question of an Increase of Atmospheric CO2 during the Past Decades. *Tellus* **9,** 18–27. doi:10.1111/j.2153-3490.1957.tb01849.x (1957).

Supplementary file for "Resolved tropical cyclones trigger CO_2 uptake and phytoplankton bloom in Earth system model simulation"

David M. Nielsen[1*], Fatemeh Chegini[2], Nuno Serra[2], Arjun Kumar[1], Nils Brüggemann[1], Cathy Hohenegger[1], and Tatiana Ilyina[1,2,3]

[1]Max Planck Institute for Meteorology, Hamburg, Germany

[2]Universität Hamburg, Hamburg, Germany

[3]Helmholtz-Zentrum Hereon, Geesthacht, Germany

[*]Correspondence to david.nielsen@mpimet.mpg.de

March 18, 2025

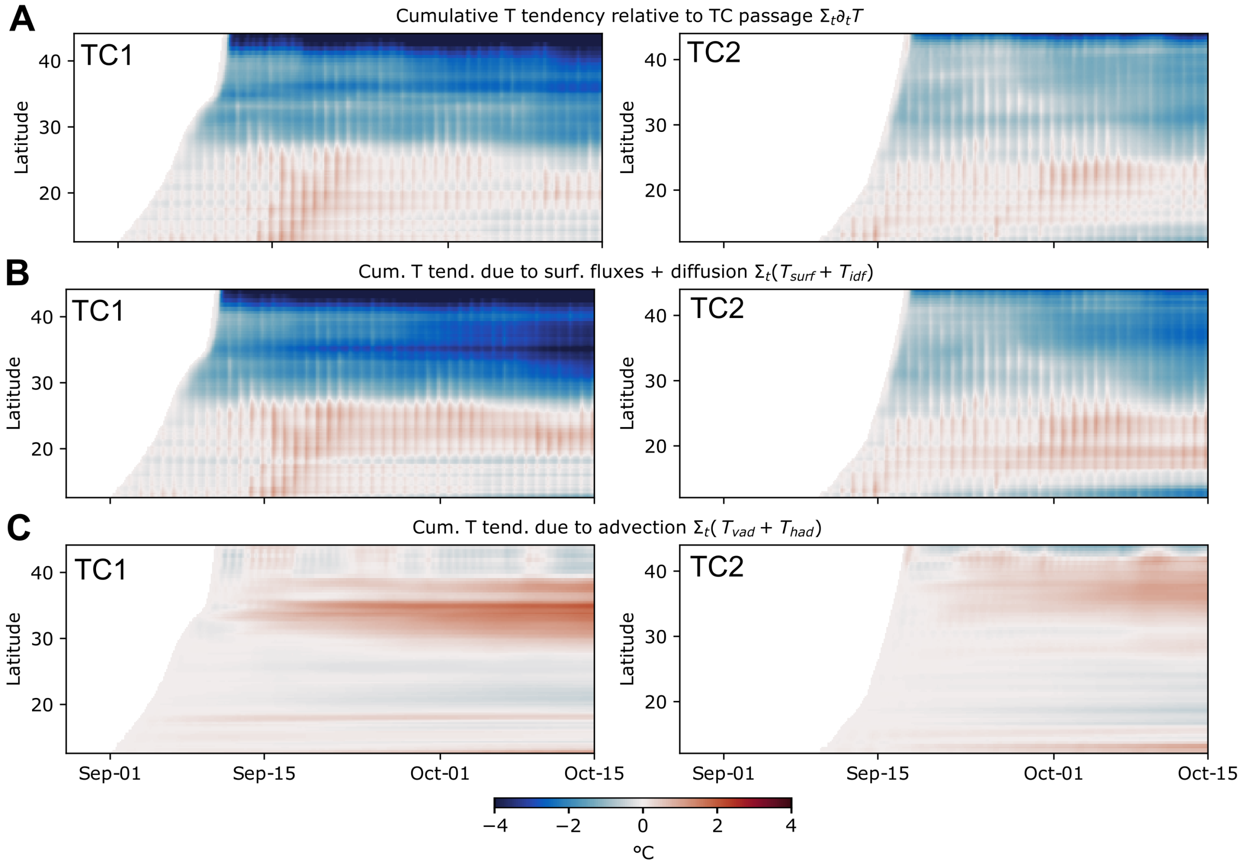

Figure S1: Changes in sea-surface temperature (SST) relative to the passage of TCs. Total change in SST **(A)**, expressed as accumulating temperature tendencies from 12 hours before the TC passage, cumulative tendency terms due to the isolated effects of surface heat fluxes and vertical diffusion by turbulent mixing **(B)**, and due to the effects of vertical and horizontal advection **(C)**.

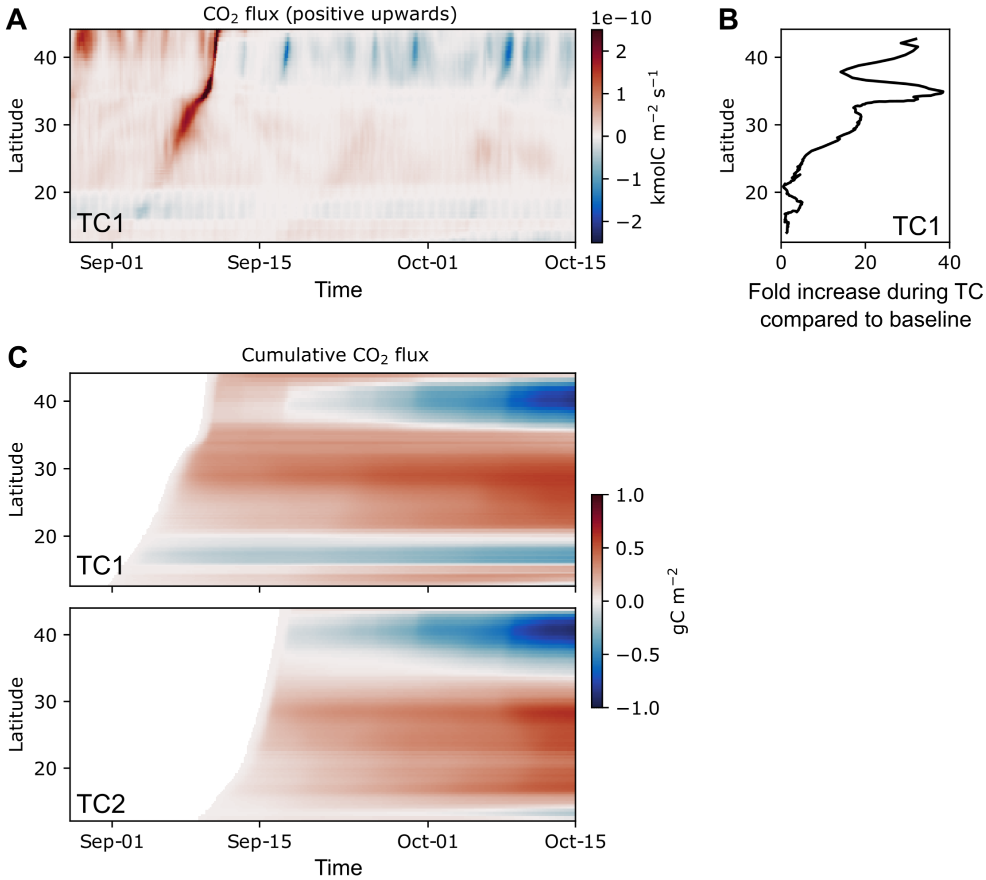

Figure S2: Impact of TCs on air-sea CO_2 fluxes. Along-track time series of air-sea CO_2 fluxes averaged over a 200-km radius from the TC center (here as in Fig. 2 in the main text, but for TC1) **(A)**, ratio between magnitude of air-sea CO_2 flux during TC1 and baseline, which here is the 1-month period from Oct-1 and Oct-31 excluding the TC days **(B)**, and the cumulative air-sea CO_2 flux starting at 12 hours prior to the TC passage at each location along their tracks **(C)**. A switch from positive to negative cumulative flux in (C) indicates the moment when the CO_2 uptake following the TC passage outweighs the outgassing triggered during their passage.

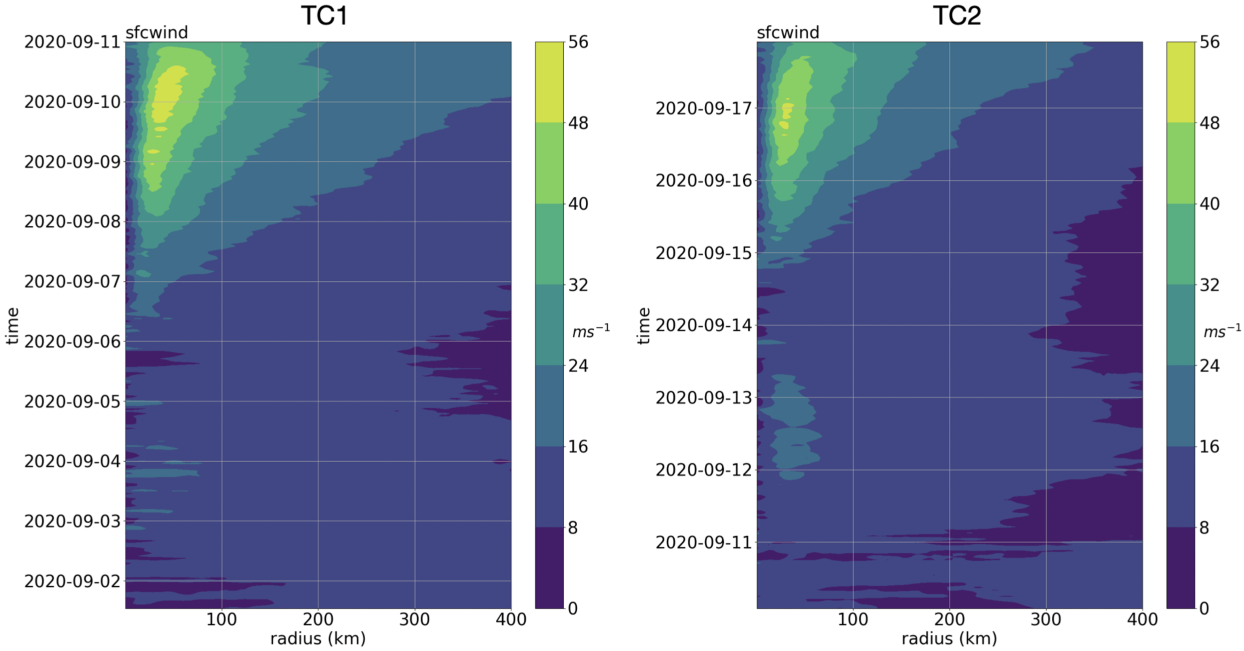

Figure S3: Temporal evolution of surface wind speeds along the track of TC1 (left) and TC2 (right) as a function of radial distance from cyclone center.

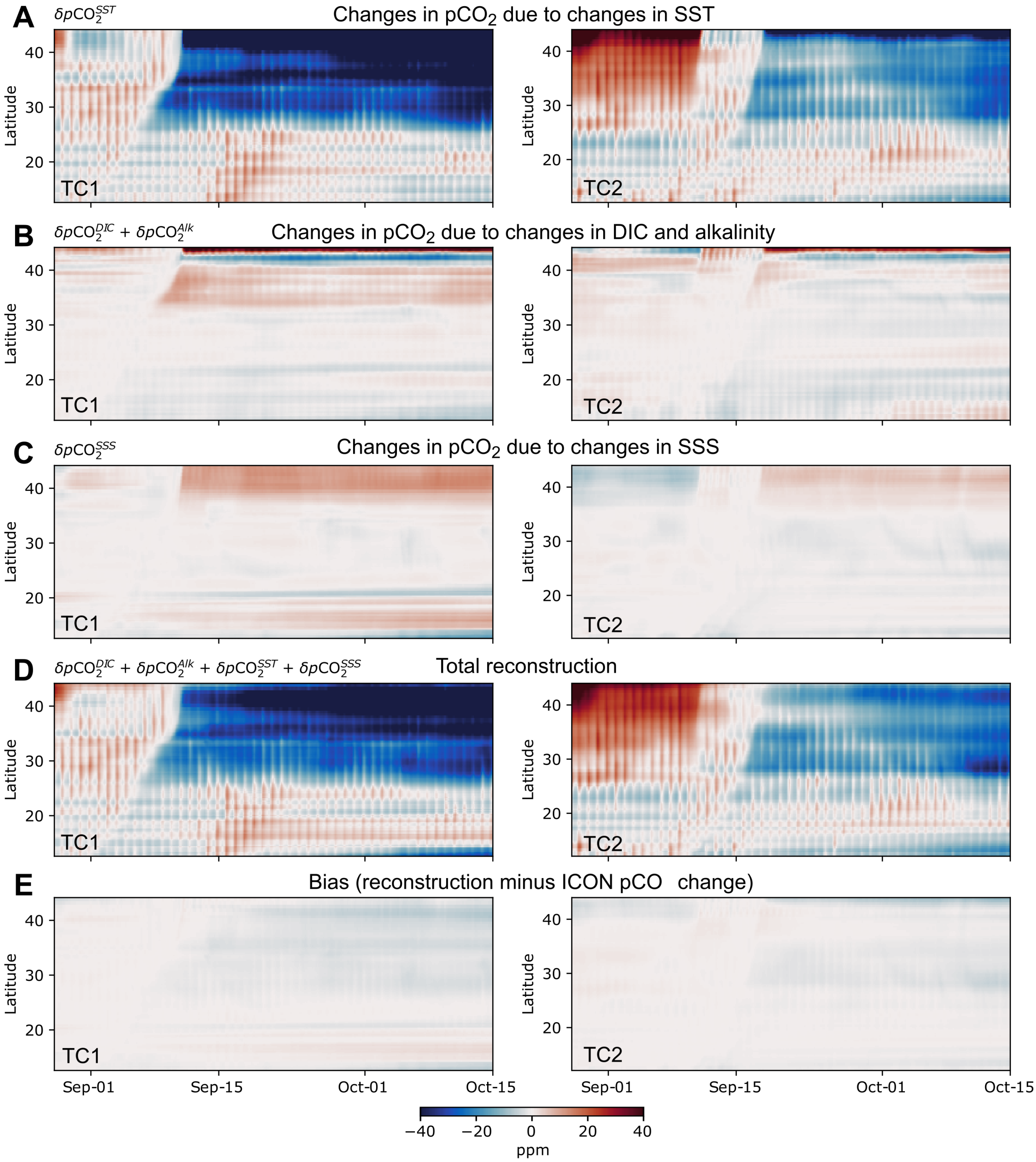

Figure S4: Along-track time series of changes in pCO_2 due to changes in sea-surface temperature (SST, **A**), DIC and alkalinity (**B**), sea-surface salinity (SSS, **C**), their reconstructed combined effect (**D**), and the difference between this reconstruction and the pCO_2 changes simulated directly with our model (reconstruction bias, **E**). On the left-hand-side are shown time series along the track of TC1, while on the right-hand-side are shown time series along the track of TC2.

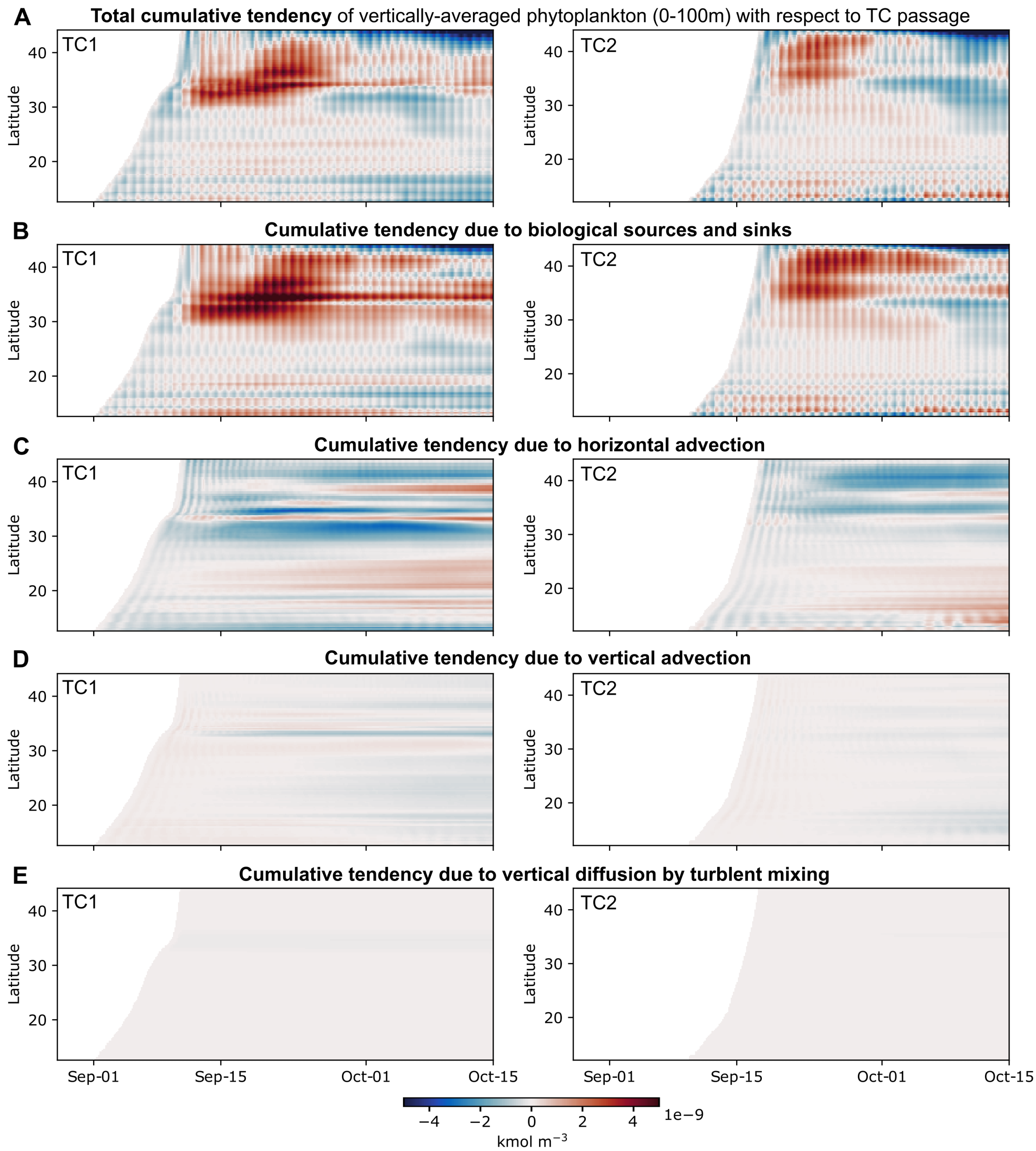

Figure S5: Along-track time series of cumulative tendencies of integrated (0-100 m) phytoplankton concentrations **(A)** and its components, that is, changes in phytoplankton concentrations due to biological sources and sinks **(B)**, horizontal advection **(C)**, vertical advection **(D)**, and wind-driven vertical diffusion by mixing **(E)**. Accumulating periods start 12 hours before the TCs passage.

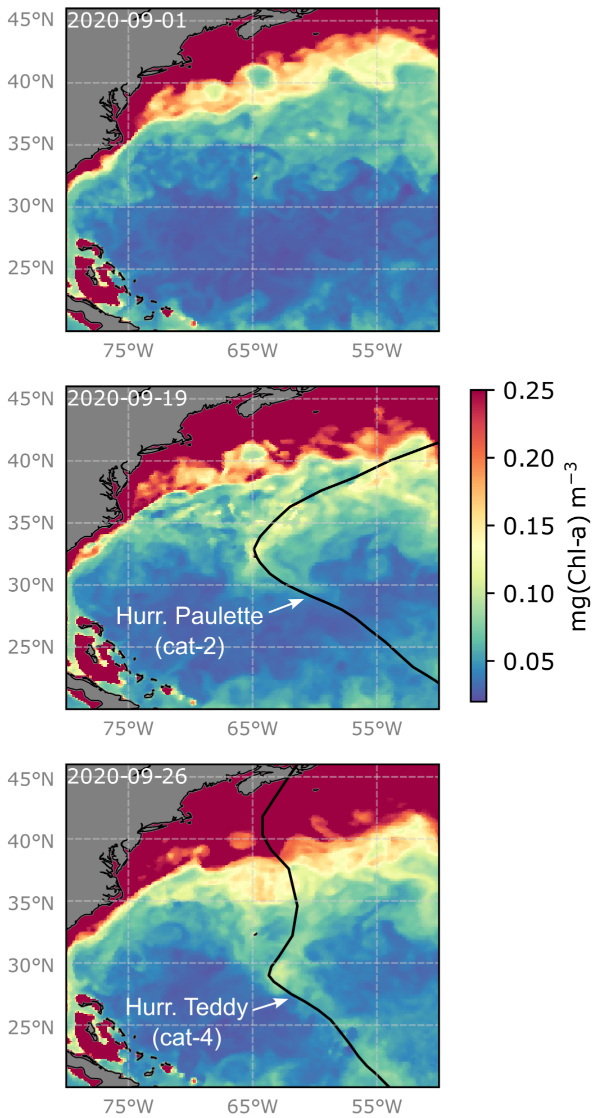

Figure S6: Satellite-derived Chlorophyll-a observations on 01-09-2020, 19-09-2020, and 26-09-2020, overlaid with the tracks of TCs Paulette and Teddy. TC Paulette reached peak intensity to hurricane category 2 on 10-09-2020 , and made landfall in Bermuda on 14-09-2020. TC Teddy reached peak intensity on 17-09-2020 to hurricane category 4. Black lines show the TC tracks. Chlorophyll-a data are obtained from [1], and TC tracks are obtained from NOAA's Atlantic hurricane database (HURDAT2) [2].

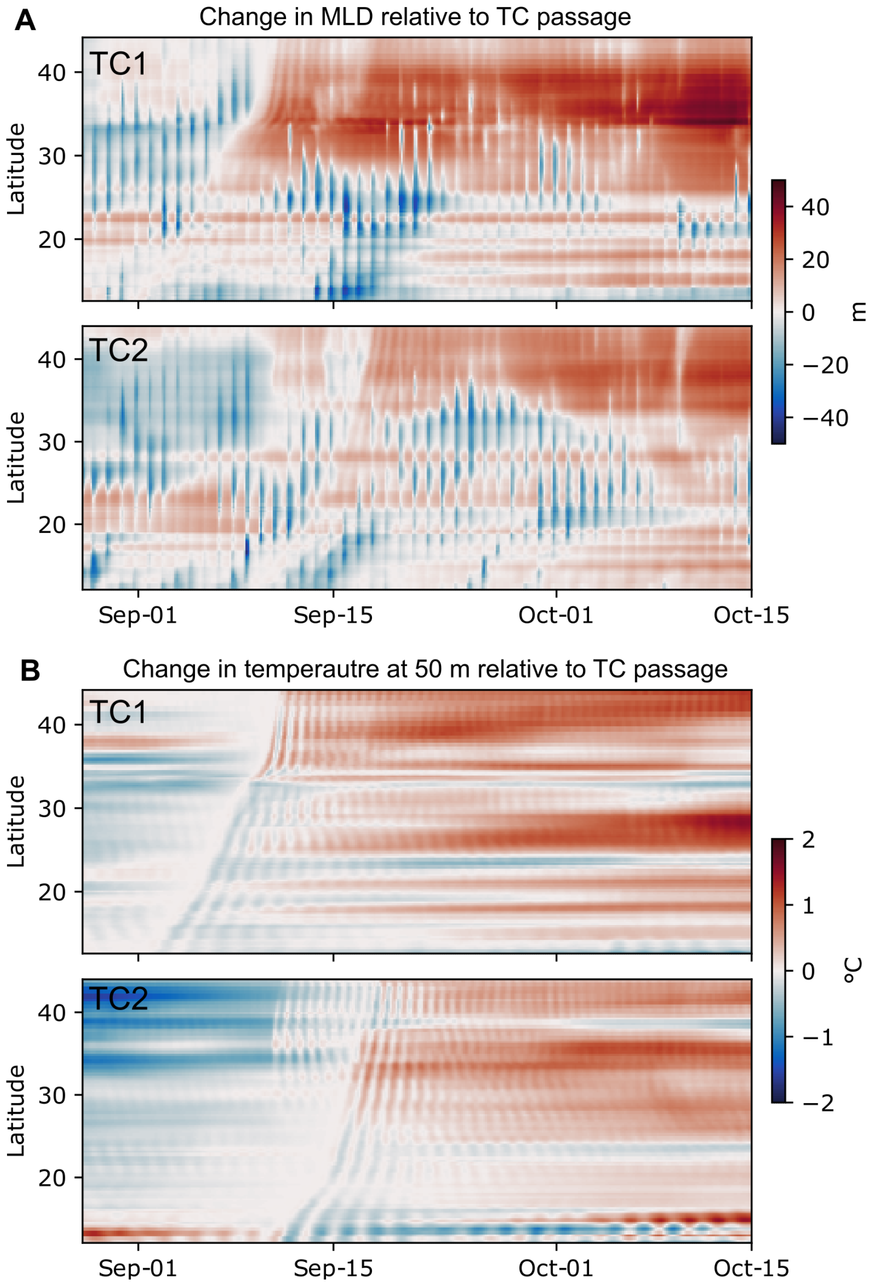

Figure S7: Along-track time series of changes in mixed-layer depth (MLD, **A**) and in temperature at 50 m (**B**) with respect to the passage of TCs.

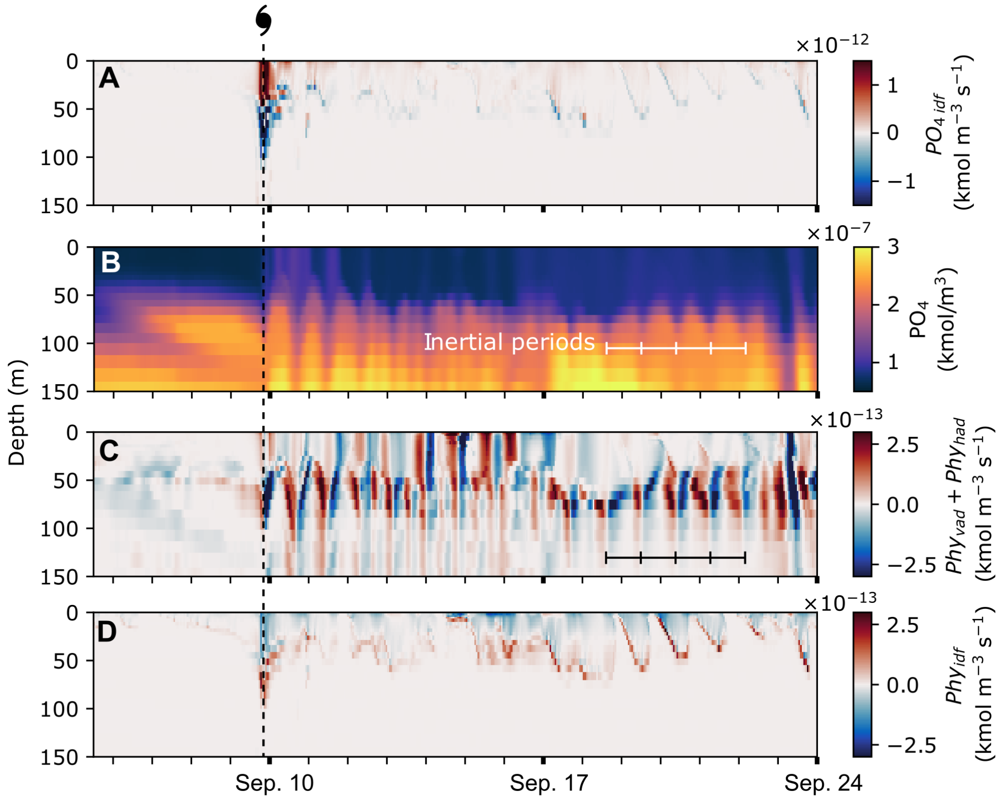

Figure S8: Time series at 37°N 67°W, continuation of Fig. 4 in the main text. Here shown are changes in phosphate concentrations due to vertical diffusion by wind-driven mixing **(A)**, phosphate concentrations **(B)**, changes in phytoplankton concentration due to horizontal and vertical advection **(C)** and due to vertical diffusion by mixing **(D)**

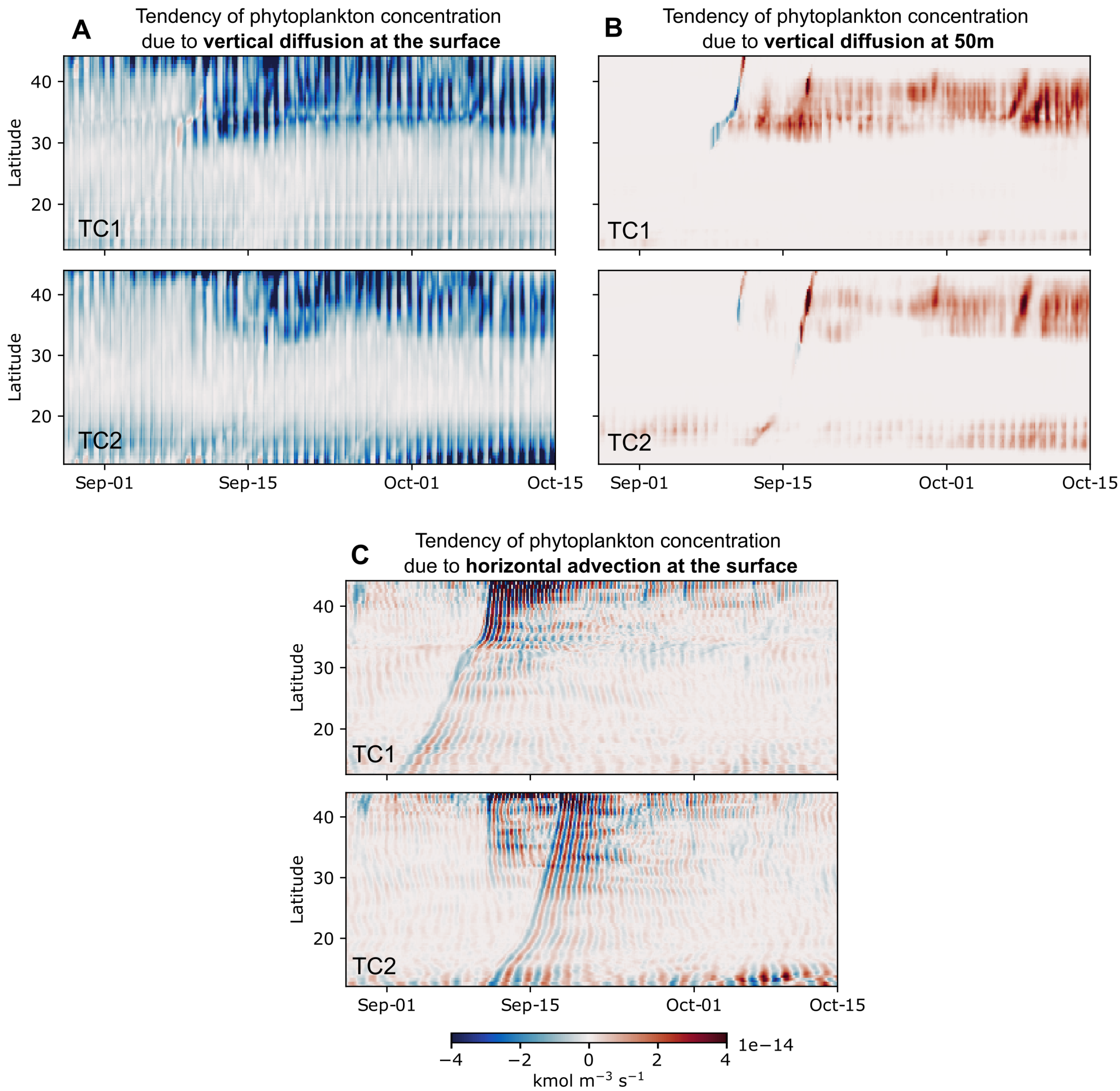

Figure S9: Along-track time series of changes in phytoplankton concentration due to horizontal advection and vertical diffusion. Quantities are averaged from a 150 km-radius circle following the center of the TCs along their tracks. The left vertical axes show the along-track distance from the first point where the TC is detected. The right vertical axes show the latitude coordinate of the center of TCs along their tracks. The vertical advection components of phytoplankton tendency show a similar pattern to those of horizontal advection, but with opposite sign, due to continuity. Note the dominant role of inertial oscillations, and their increasing frequency with latitude, in the variability of the advection terms. Data are *not* filtered.

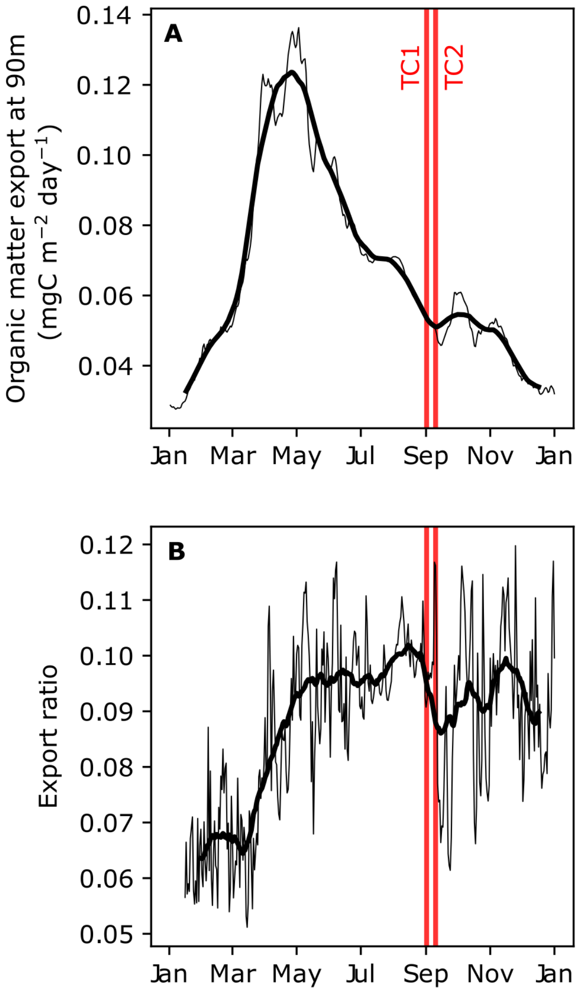

Figure S10: A) seasonal cycle of organic matter export at 90m averaged over the western North Atlantic (triangular region in Fig. 3A), and **B)** the ratio between organic matter export and NPP in this same region. Thin lines show daily means, and thick lines show 31-day running means of daily means. The passage of our simualted TCs are marked by the red bars.

References

1. Liu, X. & Wang, M. Global daily gap-free ocean color products from multi-satellite measurements. *International Journal of Applied Earth Observation and Geoinformation* **108,** 102714. ISSN: 1569-8432. doi:`https://doi.org/10.1016/j.jag.2022.102714` (2022).

2. Landsea, C. W. & Franklin, J. L. Atlantic Hurricane Database Uncertainty and Presentation of a New Database Format. *Monthly Weather Review* **141,** 3576 –3592. doi:`10.1175/MWR-D-12-00254.1` (2013).